International Journal of Hydrogen Energy 65 (2024) 292–307

Contents lists available at ScienceDirect

International Journal of Hydrogen Energy

journal homepage: www.elsevier.com/locate/he

Revealing the critical role of low voltage excursions in enhancing PEM fuel cell catalyst degradation by automotive hydrogen/air potential cycling experiments

Elena Colombo [a,*], Andrea Casalegno [a], Laure Guetaz [b], Andrea Baricci [a]

[a] Politecnico di Milano, Department of Energy, Via Lambruschini 4, 20156, Milano, Italy
[b] CEA, LITEN, Université Grenoble Alpes, 17 Rue des Martyrs, 38054, Grenoble, France

ARTICLE INFO

Handling Editor: Dr Mehran Rezaei

Keywords:
Proton exchange membrane fuel cell
Catalyst degradation
Accelerated stress test
Voltage cycling
Short-stops
Nanoparticles growth

ABSTRACT

The durability of Polymer Electrolyte Membrane Fuel Cells under dynamic operation still needs to be improved. To understand the automotive voltage cycling-induced catalyst degradation, the loss of the electrochemically active surface area (ECSA) is investigated through an experimental campaign on Membrane Electrode Assemblies. Ad-hoc hydrogen/air accelerated protocols were designed to evaluate the voltage profile impact in a range relevant for both automotive and heavy duty transport application (<0.90 V). Besides the well-known aging dependence on the upper potential limit, this work evidences the critical role of the short-stops, characterized by low voltage transients. Effort was spent in studying this procedure parameters (voltage level, duration, scan rate, humidification). The accelerated ECSA loss is due to Pt nanoparticles coarsening as proved by transmission electron microscopy and is suspected dominated by Pt cathodic dissolution, incentivized during excursions towards very low potentials (<0.4 V). These findings help the development of system mitigation strategies.

1. Introduction

1.1. State of the art

There is an urgent need for sustainable technological solutions to face the environmental challenges. Fuel cell electric vehicles are a promising technology for reducing the pollutants emissions of the transportation field. Among the different fuel cell types, Proton Exchange Membrane Fuel Cells (PEMFC) are considered as the most mature for being applied in both passenger and heavy-duty vehicles [1]. Nonetheless, fundamental and applicative research is still necessary to overcome some technical barriers [2], which are the cost and degradation.

One of the most relevant contributors to the loss of performance is the degradation of the cathode catalyst layer [3]. This component consists of catalyst nanoparticles (made by Pt or Pt-alloy) supported on carbon and covered by ionomer. In particular, the electrochemically active surface area (ECSA) of the catalyst is lost over time. This can be the consequence of many mechanisms that alter the Pt nanoparticles (NPs), like their coarsening, coalescence and detachment [4,5], and of alterations of ionomer and support (e.g. due to its corrosion [6]). During fuel cell vehicles operation, characterized by thousands of operating hours under a variable load, both high potentials and potential cycles were identified at the origin of aging [7]. Indeed, they are responsible of Pt dissolution under the acidic environment of the cathode catalyst layer. The smaller Pt nanoparticles dissolve faster due to the negative shift in the equilibrium potential of their dissolution reaction [8], in analogy to the Gibbs-Tomson relation. The formed Pt ions then precipitate upon larger particles (electrochemical Ostwald ripening mechanism) or into the electrolyte phase after diffusion towards the membrane, where they are reduced by the crossover hydrogen to form the Pt precipitate band [9]. In dynamic conditions, voltage fluctuations cause repetitive surface oxidation and reduction of the Pt nanoparticles. This mechanism is known to strictly interact with the dissolution process [10–12]. However, there are different theories about the role of the Pt oxides into dissolution. On one hand, it is recognized a passivating effect of the Pt surface that acts therefore as a protective layer, inhibiting the anodic dissolution (i.e. steady-state or transient dissolution from the Pt surface, that dominates during anodic transients). On the other hand, studies suggest a second, opposite role, considering some forms of oxides as directly susceptible to Pt dissolution or indirectly responsible of it when they are reduced. The former process is identified as chemical

* Corresponding author.
E-mail address: elena.colombo@polimi.it (E. Colombo).

https://doi.org/10.1016/j.ijhydene.2024.03.373
Received 13 January 2024; Received in revised form 8 March 2024; Accepted 31 March 2024
Available online 6 April 2024

dissolution, enhanced at high potentials when the coverage is high, while the latter is indicated as cathodic dissolution (i.e. transient dissolution process from a "place-exchanged" platinum oxide subjected to a cathodic treatment). Ahluwalia et al. [13] proved that the cathodic dissolution greatly exceeds the anodic in cycling at an Upper Potential Limit (UPL) above 0.90 V, by adopting a flow cell and an on-line inductively coupled plasma mass spectrometer (ICP-MS). Even though the valuable interpretation provided by this fundamental analysis, the setup cannot fully agree with the complexity of the fuel cell device [14] that requires dedicated studies closer to the real-world configuration.

Nanoparticles growth is dependent on a wide number of factors [15], as Pt nanoparticle size and distribution [16]. In addition to material properties, operating parameters are of a high relevance [17]. The conditions that promote catalyst degradation were studied in accelerated stress tests (ASTs). High relative humidity (RH) [18] and temperature [19,20] dissolve more rapidly the nanoparticles, since they incentivize the kinetics of Pt dissolution and oxide formation reactions; furthermore, a higher water content makes more rapid the Pt ions transport. One of the most important parameters is the UPL of the voltage cycles: its increase incentivizes the ECSA loss rate [21,22]. The shape of the cycling profile affects the Pt durability too. Uchimura and Kocha [23] concluded that square waves are more damaging rather than triangular. Concerning the impact of the lower potential limit (LPL), only a few results have been instead reported [23,24], but the potentiality of exploiting this parameter to reduce the degradation has recently risen of high interest [25].

1.2. Aim of the work

For deepening the comprehension of the ECSA loss, this work presents the results of different voltage-cycling profiles in hydrogen/air atmosphere applied on commercial Membrane Electrode Assemblies (MEA's). An automotive representative AST, presented in a previous publication [26], was selected as the starting point of this work. After the application of this aging protocol, the cathode catalyst layer was observed as the mostly aged component, consistently to the degradation induced by a long-term operation (1000 operating hours) discussed into details in an earlier paper [27]. The electrochemical Ostwald ripening mechanism was detected as the main origin for catalyst aging.

Here, this AST was modified to obtain ad-hoc experiments able to clarify the main stressors accountable for the decay of the Pt active surface area. The investigation focuses on operating conditions relevant for real systems and was thus restricted to the voltage window accessible by the fuel cell. In agreement with the applicative strategies that prevent Open Circuit Voltage (OCV), the cell potential did not go beyond 0.85–0.90 V. Furthermore, the short-stop procedure [27–29] was included, which makes the voltage drop to values lower than 0.1 V, since the air flow is not supplied. In this way, the most frequent potential transients that are likely occurring in systems are fully comprised. This is a source of originality of this work, since the electrocatalyst ASTs usually exploited are signed by potential profiles up to 0.95–1 V and limit the minimum voltage to 0.6 V [30]. In addition, the catalyst degradation was trigged in hydrogen/air or diluted air atmosphere to be as much realistic as possible. The importance of shifting accelerated protocols from an inert atmosphere [31] to the regular fuel cell operational environment is currently reported in many researches [26,32]. Nevertheless, only a limited number of papers exploited air ASTs for a parametric stressors study [33–35] and the impact of gas composition is still under debate. It is worth noting that the air adoption keeps track of the *operando* MEA performance, providing insights into the aging interpretation. The testing campaign was thought to assess the role of both the voltage range and transitions, for a total of 30 tested samples.

Since the main objective of the work is to study the impact of short-stops on catalyst degradation, their critical role is first presented in Section 3.1. Then, with the purpose to clarify which is the voltage profile characteristic responsible for the promotion of the aging, a parametric analysis was dedicated to investigate both the short-stop properties and the operational history, as exemplified in Fig. 1A and Fig. 1B. Parameters connected to the short-stop have been detailed, as the short-stop potential (Section 3.2), its regulation, in terms of scan rates and duration (Section 3.3), and its humidification (Section 3.4). Among all, we identified the short stop potential as a relevant parameter, thus a supplementary analysis on the low voltage transitions was pursued, which comprised more frequent transients (Section 3.2.1). Regarding the operational history, the profile under the operative time was modified to track the influence of the UPL (Section 3.5), the number of cycles (Section 3.6) and the cathode gas feeding composition (Section 3.7). Overall, the findings provide a broad picture of the short-stop influence and they are of hint for the development of system mitigation strategies.

2. Experimental methodology

The details related to the experimental methodology can be found in previous publications [26,27,36]. The most relevant information are summarized in the following for readability purposes.

2.1. Materials and equipment

Two Catalyst Coated Membranes (CCM's) were tested and indicated as I and II. They consist in commercial Pt/C materials provided by two manufactures: CCM I has 0.1/0.5 mg cm^{-2} Pt loading, while CCM II is signed by 0.1/0.4 mg cm^{-2} Pt loading, both based on 18 μm-thick PEM (reinforced and chemically stabilized by radical scavenger) [26]. Cathode electrode carbon support is graphitized and its thickness is 15 ± 3 μm for CCM I and 10 ± 2 μm for CCM II. The CCM I Pt/C loading is in the range 40–60 wt %. The anode catalyst layer thickness is almost 5 μm for CCM I and 3 μm for CCM II. The 2 cm^2 MEA's combined these CCM's with gas diffusion layers supplied by Freudenberg (H14CX483). The samples were mounted using quasi-incompressible gaskets (Mylar®) to obtain a compressed thickness which was the 80% and 81% of the uncompressed, for CCM I and CCM II respectively [26]. The MEA's were assembled in the hardware at a torque of 9 Nm.

All measurements were performed on a customized test station using a zero-gradient cell hardware. The hardware, characterized by parallel channels, was configurated to operate with high stoichiometry (8/20 at anode/cathode) to keep uniform working conditions. Its open source design is provided in the work by Colombo et al. [37] and used to the simultaneous test of four CCM's. A detailed description of the test station equipment was reported in a previous paper [26], which the reader could refer to. The adoption of a multichannel load granted to control the accelerated protocol voltage profile for each single MEA. Protocols were designed in LabView® environment.

2.2. AST procedures and MEA characterization measurements

The experimental procedure is depicted in Fig. 1C. All MEA's were conditioned prior to testing, switching the current every 2 min (0.2–0.8 A cm^{-2}) for 17 h [26,27]. A H_2/N_2 OCV period is introduced every 20 cycles of the break-in protocol, which is performed at 65 °C and at full humidification.

Before each set of diagnostic measurements, an MEA recovery step was implemented. It consists in two separated steps: (*i*) first, in only supplying air at the cathode compartment to allow O_2 to diffuse towards the anode, where no gas is fed, for a total of 15 min. The procedure mirrors a realistic system long stop and it is helpful for anode reactivation [26]; (*ii*) second, in performing at 30 °C and for 10 times a 100 mV s^{-1} cyclic voltammetry to high voltage (OCV-1.20 V_{RHE}); the protocol strips catalyst contaminants and ensures a better reproducibility of the subsequent cyclic voltammograms used for determining the ECSA, the main parameter under analysis. ECSA was evaluated from CV at 30 °C, 100 mV s^{-1} and limiting the upper potential to 0.6 V_{RHE}, by averaging the H-desorption charge of five consecutive scans. A 210 μC

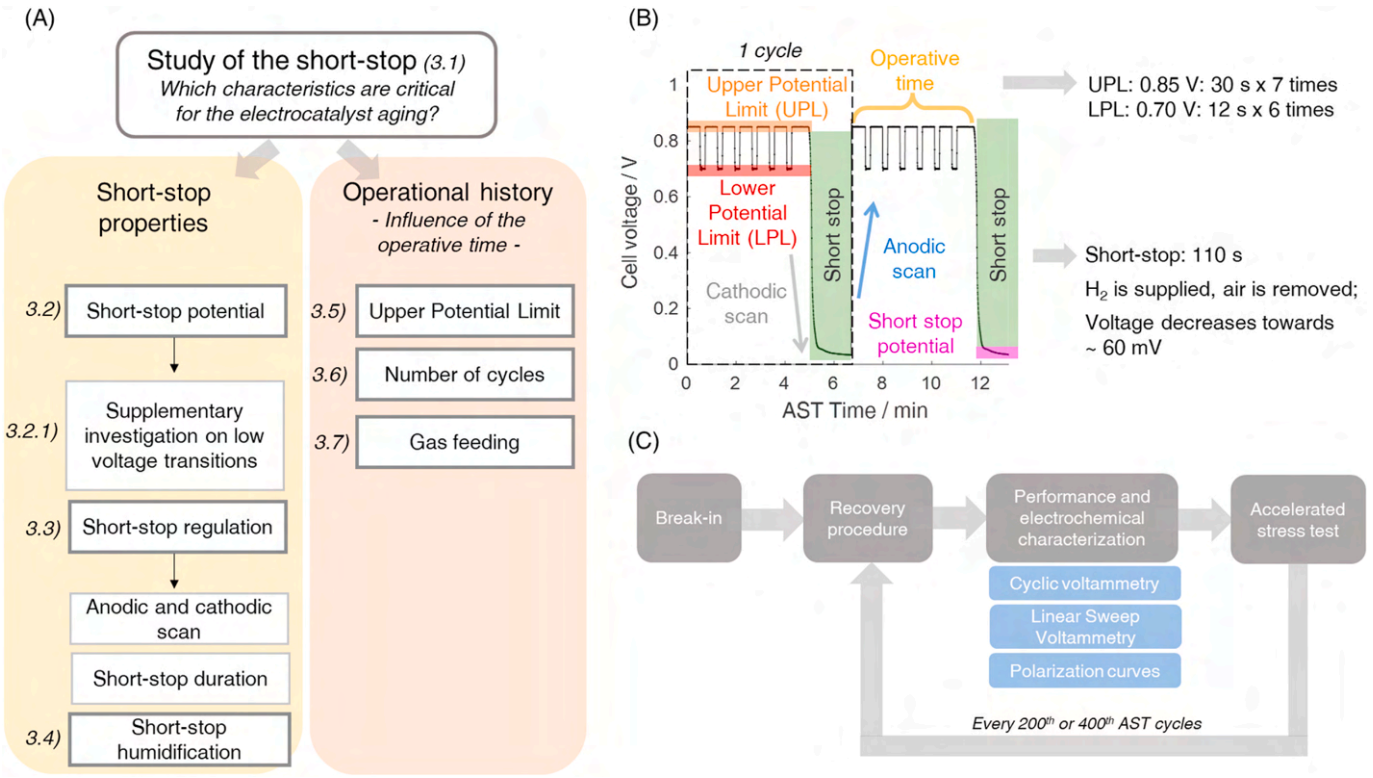

Fig. 1. (A) Aim of the work and rationale: the short-stop role is pursued in dependence on both short-stop properties and operational history (i.e. characteristics of the operative time). The presence/absence of short-stops is investigated, as well as the short-stop potential, its regulation and humidification. Among all, the highlighted critical role of the short-stop potential required to further investigate the low voltage transitions. On the other hand, characteristics of the operative time were changed, as the UPL, the number of cycles and the gas feeding composition to assess their interaction with the degradation induced by stopping. The number of the section where the results are included is reported besides each stressor; (B) Accelerated Stress Test profile that mimics the low power operation in presence of short-stops. The profile is adapted from the protocol proposed in a previous publication [26]. The influence of the highlighted parameters is quantified in this work. 1 AST cycle corresponds to 6 cycles in the operational window (4.7 min), followed by a short-stop (110 s). The "AST time" corresponds to the time of the whole protocol; (C) Scheme of the experimental procedure for studying MEA degradation under AST.

cm^2_{Pt} specific charge is assumed. Anode and cathode electrodes were fed by fully humidified 100 NmL min^{-1} hydrogen and nitrogen streams respectively. Alongside ASTs application, the features related to the hydrogen adsorption/desorption (region below 0.4 V) decreased because of the reduction of the catalyst roughness factor (rf) [cm^2_{Pt} cm^{-2}_{geo}], from which the ECSA [m^2_{Pt} g^{-1}_{Pt}] is computed hypothesizing an unchanged Pt loading.

As included in another authors' work [26], the reference polarization curve was registered in current-control mode at 80 °C and fully humidified gas feedings. Each current density point of the polarization curve lasted 180 s, of which the first 30 s were discarded to quantify the average voltage. The protocol consisted in increasing the current density from 0.005 A cm^{-2} up to 4 A cm^{-2}, and then in reducing the values with the opposite trend. As a standard for comparing the results and studying the CCM degradation, the advancement from high to low currents was selected [38]. Stoichiometry was set to 8/20 at anode/cathode, while the minimum flow was the equivalent at 0.5 A cm^{-2}. Inlet pressure was 250/230 kPa_{abs} at anode/cathode. Prior to recording a polarization curve, the cell was held at 0.5 A cm^{-2} for 5 min. Electrochemical Impedance Spectroscopy (EIS) measurement was implemented during the polarization protocol, both at 1 A cm^{-2} and at 3 A cm^{-2}.

Aging of the cathode electrodes was obtained under various voltage cycles. The potential profiles were designed starting from the Low Power AST protocol previously proposed [26], which mimics an automotive low load profile [27]. Here, we chose to apply a voltage-controlled logic to make the analysis of the voltage profile easier. Fully humidified or oversaturated conditions were selected to focus the study on the catalyst degradation and avoid possible contributions due to ionomer deterioration. The cell temperature was 71 °C and the inlet pressure was 140/190 kPa_{abs} at cathode/anode. The reference profile (Fig. 1B) consists in a period of 4.7 min ("operative time") where the voltage was cycled six times between 0.7 V and 0.85 V. The dwell time at 0.85 V was 30 s, while 12 s at 0.7 V. A short-stop followed, which lasted 110 s. The combination between this operative period and the short-stop consists in one AST cycle. The short-stop (identified as "no-air stop" in the following) consisted in the air flux interruption under a resistive control while hydrogen was supplied, as explained in other works [26,27]. In the meanwhile, the cathode reached the ambient pressure and the anode pressure was reduced to 150 kPa_{abs}. Furthermore, the quantities indicated in Fig. 1A and Fig. 1B (UPL, LPL, the number of cycles in the operative period, short-stops presence and its parameters) were varied to measure the stressing role caused by the voltage window and by the voltage transients. In all the cases, the temperatures of the cell hardware and of the bubblers were regulated under hydrogen/nitrogen prior to start the test. One hour was spent in these conditions to allow a sufficient stabilization. Then, 3 min were spent at UPL and under the gas feedings of the test (hydrogen/air or hydrogen/diluted air) to regulate the anode and the cathode pressures.

For completeness, it is noteworthy to mention that the cell voltage deviates from the cathode catalyst potential because of the actual drawn current at each time. A very simplified estimation of the cathode electrode voltage (E) was computed in this work by correcting the imposed cell potential (E_C) for the ohmic overpotential. The computation considers the average current drawn during the protocol i_j, at the j^{th} potential level of the test:

$$E = E_C + i_{j,avg} R_\Omega \quad (1)$$

$$i_{j,avg} = \frac{1}{\Delta t} \int_{BoT}^{EoT} i_j(t)\, dt \tag{2}$$

R_Ω is estimated by the High Frequency Resistance from impedance spectra at the protocol operating conditions and it was measured as equivalent to 0.025 Ω cm^2.

For describing the trend of the ECSA decay and furnishing a guide-to-eye for its evolution, the expression included in Equation (3) was exploited [39,40], which agrees with the mechanism of nanoparticles growth because of ripening:

$$\frac{dECSA}{dN} = -c^* \, ECSA^2 \exp(\omega^* ECSA) \tag{3}$$

N is the number of AST cycles, c^* is the proportionality constant and ω^* is the exponential constant. The equation can be re-arranged for expressing the normalized surface area S, defined as the ratio between the ECSA and the ECSA at BoT ($ECSA_0$):

$$\frac{dS}{dN} = -c\, S^2 \exp(\omega\, S) \tag{4}$$

Where c is equivalent to $c^* \cdot ECSA_0$ and ω to $\omega^* \cdot ECSA_0$. The expression describes the logarithmic decay of ECSA with respect to time or with respect to the protocol cycle number, a behaviour already reported in literature [41] and verified to be in good agreement with our experimental results. This equation was used for calculating a concise degradation rate k, obtained as the product between c and $\exp(\omega)$, where the values c and ω were least-squares regressed over the experimental data. Such parameter corresponds to the rate of decay at the beginning of the degradation protocol (i.e. for S equal to 1). This description physically supports the progressive stabilization of the normalized ECSA, while limiting to zero the minimum value that can be reached.

2.3. TEM and SEM analysis

Cross-sections of MEA's both at the beginning of the test and after AST cycles were prepared for transmission electron microscopy (TEM) and scanning electron microscopy (SEM) characterization. Pieces of samples were first embedded in a resin (EpoFix Struers®) then, for TEM observations, thin MEA sections were sliced by an ultramicrotome (LEICA). Images were taken using a FEI-Titan microscope which adopts a Cs image corrector. The diameters of the spherical Pt NPs were manually measured and the size distribution histograms finally reconstructed [26,27]. Then, it was calculated: (*i*) the average volume/area diameter $\overline{d}_{v/a}$, obtained from Equation (5) [42], (*ii*) the Geometric Surface Area (GSA), which is expressed by Equation (6), (*iii*) the catalyst utilization factor (u.f.) from Equation (7), (*iv*) the mean diameter $\overline{d}$, equivalent to the simple arithmetic average of the measured diameters.

$$\overline{d}_{v/a}[nm] = \frac{\sum_i d_i^3}{\sum_i d_i^2} \tag{5}$$

$$GSA\left[\frac{m^2}{g}\right] = \frac{6}{\rho_{Pt}} \frac{1}{\overline{d}_{v/a}} \tag{6}$$

$$u.f. = \frac{GSA}{ECSA} \tag{7}$$

The SEM analysis was instead performed with a Zeiss EVO 50 SEM, equipped with energy-dispersive x-ray spectroscopy microprobe. Backscattered electrons were employed to evidence the cross-section features, thanks to the compositional differences, after having mechanically polished the sample to obtain a mirror-like surface.

3. Results and discussion

3.1. The role of short-stop

The short-stop is a frequent stop procedure for an automotive fuel cell electric vehicle, introduced one every half an hour according to the ID-FAST project data [29] and similarly Takahashi et al. [43] reported an incidence of five stops a day. To assess the impact of the short-stop on catalyst aging, the protocol drawn in black in Fig. 2A was repeated on both CCM I and CCM II and compared against when it is removed, namely, substituted with an holding period at 0.7 V (yellow profile). The protocols were carried out at 6.5% $x_{O2,dry}$, whereas the no-air short-stop is periodically performed. The results of the Pt active area evolution for the two CCM's during these ASTs are summarized in Fig. 2B and Fig. 2E respectively, while cyclic voltammograms are in Figure SI1. Both the ECSA measurements performed on the two CCM's evidenced a clear difference when the stop is executed with respect to the case it is eliminated. The profile obtained in presence of stops is analogous between the two CCM's after 1600 AST cycles: retained ECSA is equivalent to 66% for both CCM I and CCM II. The stops removal strongly diminishes the rate of loss: for CCM I, normalized ECSA jumps up to 85%, while for CCM II to 76%. It is worth noting that, even though the two CCM's confirm the stop effect, some discrepancies subsist. CCM II, indeed, shows a lower difference between the two cases.

To understand the underlaying degradation phenomena, a *post mortem* TEM analysis was carried out on both the samples aged under 1600 cycles of the accelerated protocol with short-stops. The TEM images of Fig. 2C and 2F clearly show the disappearance of the smaller nanoparticles and the growth of larger. On the other hand, the carbon support not evidently corroded, since it was observed no thinning of the cathode catalyst layer and no porous structure collapse (Figure SI2A and Figure SI2B). Furthermore, no signs of Pt band formation inside the membrane and Pt depletion in the catalyst layer were found (Figures SI3 and SI4). The absence of precipitated Pt is consistent to our previous works [26,27] that investigated aging under comparable operational protocols, but not under fully humidified conditions as these cases. Additional considerations on these points are reported in Section 3.5, where the impact of the upper potential limit during the operation is discussed. The cathode electrode degradation is hence considered dominated by the electrochemical Ostwald ripening mechanism, as later corroborated by the irreversible performance loss analysis of Section 3.8. This is reasonable since carbon corrosion is expected very limited in case of graphitized support under the studied UPL (0.85 V) and at the quite low temperature (71 °C) [41,44]. In addition, the combination of the hydrogen/air environment [45] and of the voltage clipping strategy inhibits the flux of catalyst ions towards the membrane [46,47].

The particle size distribution histograms of Fig. 2D and 2G were built from TEM images. The values extracted from these histograms and the ECSA are summarized in Table 1. For CCM I, $\overline{d}_{v/a}$ grew from 4.8 nm to 7.2 nm and the utilization factor minorly varied, progressing from 70% to 71%. At the opposite, the initial $\overline{d}_{v/a}$ of CCM II is significantly lower and equal to 3.2 nm and increased to 5.5 nm. The smaller particles size of this second CCM could be at the origin of the larger rate of decay for the no-stop case, since they would dissolve more rapidly. In presence of no-air stops, the analysis of the *post mortem* images put into evidence the larger GSA drop for the smaller Pt NPs: 41% for CCM II *versus* 33% for CCM I. The change of the Pt utilization factor of CCM II, which increased from 57% to 64% (Fig. 2G), makes the ECSA decay less prominent. This observation is consistent to other literature measurements that reported that the Pt u.f. improves as the nanoparticles age and grow, most of all for the smallest (<4 nm): the trend could be ascribed to more efficient interfaces between Pt, carbon and ionomer phases consequence of the increase in size [48]. Finally, the unlike final average diameter $\overline{d}$ of the two CCM's (6.3 nm for CCM I, 4.8 nm for CCM II) may be attributed either to a different "quasi-stable" Pt NP distribution or to a different

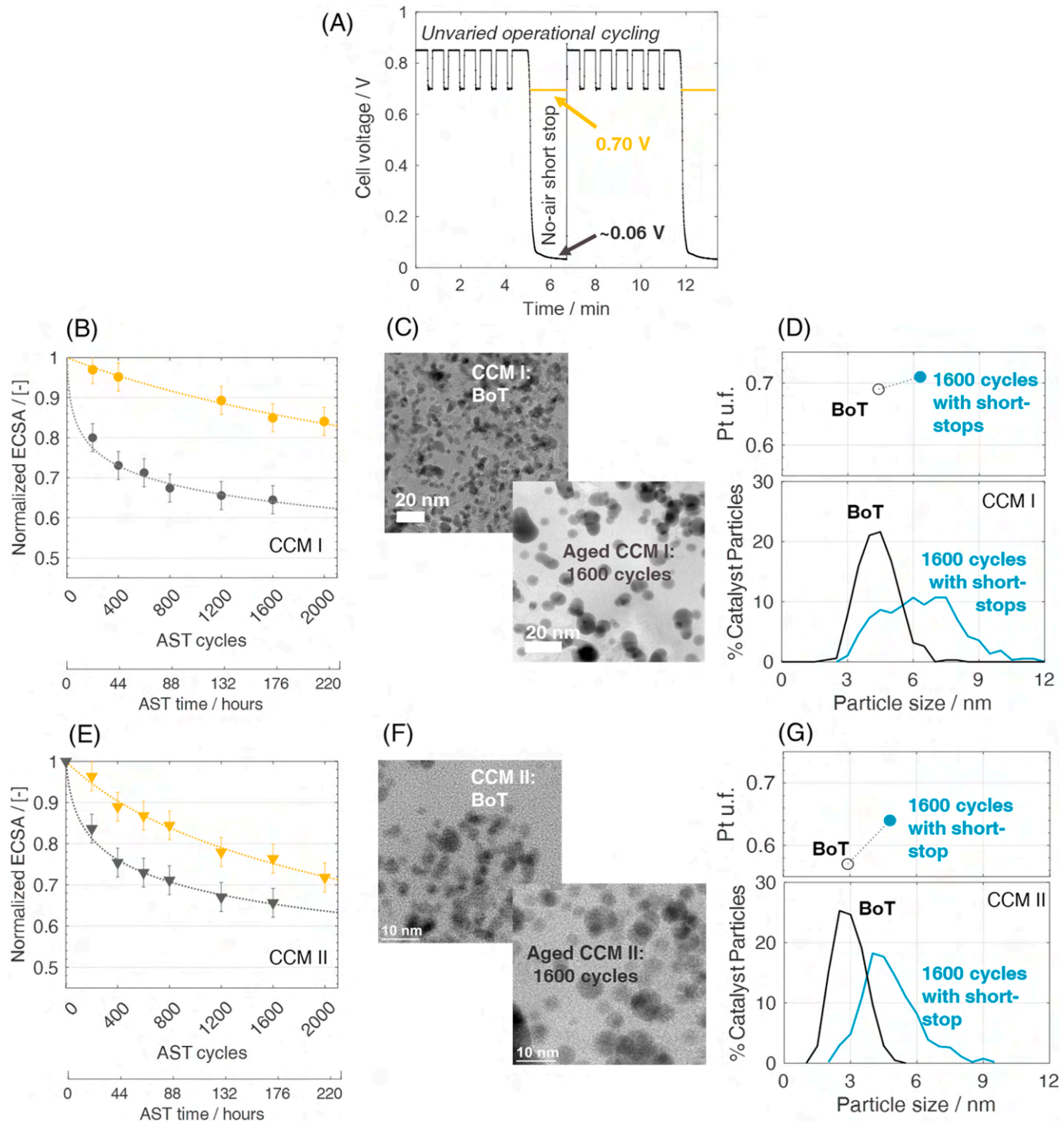

Fig. 2. (A) Voltage profile of the tested Accelerated Stress Test protocols with (black) and without (yellow) the no-air short-stops, which involve a transition to almost 0 V. When the short-stop is removed, it is substituted by an holding period at 0.7 V; (B) Normalized ECSA decay with respect to the AST cycle number and time for CCM I; (C) TEM images of CCM I cathode catalyst layer at BoT (after break-in procedure) and after 1600 cycles of AST with short-stops; (D) Pt NPs size distribution histograms of CCM I and evolution of its catalyst utilization factor (Pt u.f.) (E) Normalized ECSA decay with respect to the AST cycle number and time for CCM II; (F) TEM images of CCM II cathode catalyst layer at BoT (after break-in procedure) and after 1600 cycles of AST with short-stops; (G) Pt NP size distribution histograms of CCM II and evolution of its catalyst utilization factor (Pt u.f).

rate under which such a condition is finally got, that may be the result of multiple factors related to the physicochemical properties of the catalyst layer other than the initial nanoparticles size (e.g. support characteristics, interparticle distance and ionomer content).

As a conclusion, we proved that short-stops have a critical role in the real-world aging on two different commercial CCM's. The significant higher loss in presence of frequent short-stops, with respect to the conditions where the potential is kept $\geq$0.70 V, emphasizes that Pt degradation is mainly a transient process and that the sweep of the electrode potential towards the zero cell voltage is detrimental for the catalyst. This outcome prioritized the necessity to detail the parameters concerning the short-stop transition.

Table 1
Analysis of TEM images for CCM I and CCM II. Analysed samples are after break-in and after 1600 AST cycles with no-air short-stops.

	Counted particles [−]	GSA [m^2/g]	Average diameter (d) [nm]	Volume/area diameter ($d_{v/a}$) [nm]	ECSA [m^2/g]	Utilization factor [−]	GSA loss [%]	ECSA loss [%]
				CCM I				
After break-in Ref. [26]	347	58.5	4.4	4.8	41.5	0.70	–	–
AST w/ no-air short-stops	590	39	6.3	7.2	27.5	0.71	33	34
				CCM II				
After break-in	629	86	2.9	3.2	49	0.57	–	–
AST w/ no-air short-stops	538	50.5	4.8	5.5	32.5	0.64	41	34

3.2. The impact of short-stop potential and the performance evolution

Attention was paid in detailing the impact of some specific parameters of the short-stop. First of all, different stop potentials were tested, as shown in Fig. 3A. The evaluated values were 0.70 V, 0.60 V, 0.40 V and 0.20 V while the high potential cycling was kept unvaried, consisting in the six cycles between 0.85 V and 0.70 V. Differently from the no-air stop, diluted air was here supplied alongside the entire protocol to keep the control of the cell voltage. Note that this period of 110 s is fictitiously called stop in the following even though the cathode gas supply is not interrupted and the current is drawn. The oxygen dry mole fraction was set to 6.5% in nitrogen to avoid to reach extremely high currents (Table 2). Every 200 AST cycles, a long stop and the MEA characterization were performed. As discussed in Section 3.1 for CCM I, values of normalized ECSA equal to 66% and 85%, were established after 1600 AST cycles, in presence and in absence of short-stops respectively. Fig. 3B includes in-between values for the intermediate stop potentials: 70%, 77% and 79% for 0.2 V, 0.4 V and 0.6 V respectively. Fig. 3C shows instead the CCM II outcomes.

As already mentioned, CCM II has a higher rate of loss while cycling at high potentials. At 1600 cycles, retained ECSA is 76% at 0.7 V stop, 70% at 0.4 V stop and decreased to 66% at 0.2 V, which is minorly

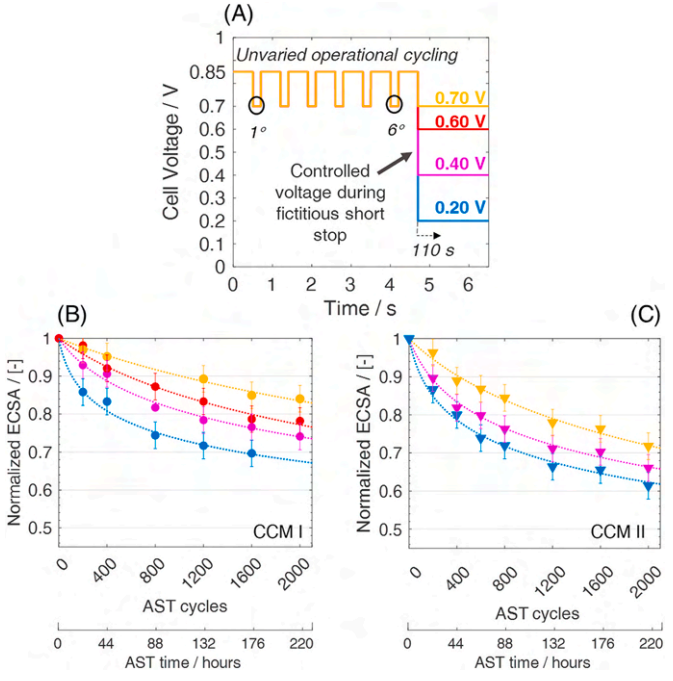

Fig. 3. (A) Voltage profile of the tested Accelerated Stress Test protocols with stops at different potentials. What included in the picture is defined as 1 AST cycle. Normalized ECSA decay with respect to the AST cycle number and operative time at different stop potentials for (B) CCM I and (C) CCM II. Different colours correspond to the profiles included in figure A.

Table 2
Table that summarizes the average current density over the whole AST protocol for dfferent fictitious short-stops potentials (carried out at 6.5% x_{O2} and at the controlled values of cell voltage E_c), the estimated cathode potential E and the rate of decay k. Results for CCM I are reported.

E_c /V	Average current density /A cm^{-2}	Estimated E /V	Concise rate of decay k /-
	Protocol with fictitious short-stop at 0.7 V		
0.85 V	0.009 A cm^{-2}	0.85 V	$1.3 \cdot 10^{-4}$
0.7 V	0.31 A cm^{-2}	0.71 V	
Short-stop at 0.7 V	0.30 A cm^{-2}	0.71 V	
	Protocol with fictitious short-stop at 0.6 V		
0.85 V	0.010 A cm^{-2}	0.85 V	$2.3 \cdot 10^{-4}$
0.7 V	0.41 A cm^{-2}	0.71 V	
Short-stop at 0.6 V	0.83 A cm^{-2}	0.62 V	
	Protocol with fictitious short-stop at 0.4 V		
0.85 V	0.018 A cm^{-2}	0.85 V	$4.6 \cdot 10^{-4}$
0.7 V	0.46 A cm^{-2}	0.71 V	
Short-stop at 0.4 V	1.23 A cm^{-2}	0.43 V	
	Protocol with fictitious short-stop at 0.2 V		
0.85 V	0.023 A cm^{-2}	0.85 V	$16.6 \cdot 10^{-4}$
0.7 V	0.52 A cm^{-2}	0.71 V	
Short-stop at 0.2 V	1.32 A cm^{-2}	0.23 V	
	Protocol with no-air short-stop (~0 V)		
0.85 V	0.010 A cm^{-2}	0.85 V	$92.5 \cdot 10^{-4}$
0.7 V	0.49 A cm^{-2}	0.71 V	
Short-stop at ~ 0 V	0 A cm^{-2}	~0 V	

different from the case of no-air stop (Section 3.1). In both the cases, we concluded that the progressive reduction of the short-stop voltage intensifies the ECSA decay. For a deeper analysis, the performance in *operando* is also considered. Fig. 4A includes the CCM I current density profile over one AST cycle at BoT (specifically, at the cycle number 20^{th}) during the operation between 0.85 V and 0.70 V. It is interestingly noting that, for the same controlled potential in the operational cycling: (*i*) the performance is boosted as the stop potential is reduced between 0.7 V and the no-air case, (*ii*) the performance variation over one AST cycle is higher as the stop potential is decreased. Indeed, the difference between the 1^{st} and the 6^{th} current points at 0.7 V (which are highlighted in Fig. 3A), monotonically raises for a lower stop voltage.

Fig. 4C and Fig. 4D depict again the information regarding the 1^{st} and 6^{th} point at 0.7 V, in this case over 1000 cycles of the AST protocol. Average data for the whole AST duration are summarized in Tables 2 and in Fig. 4B. It must be kept in mind that these profiles are the result of both reversible [49] and irreversible degradation mechanisms, mostly since both Pt oxides and ECSA are differently evolving. In addition, note

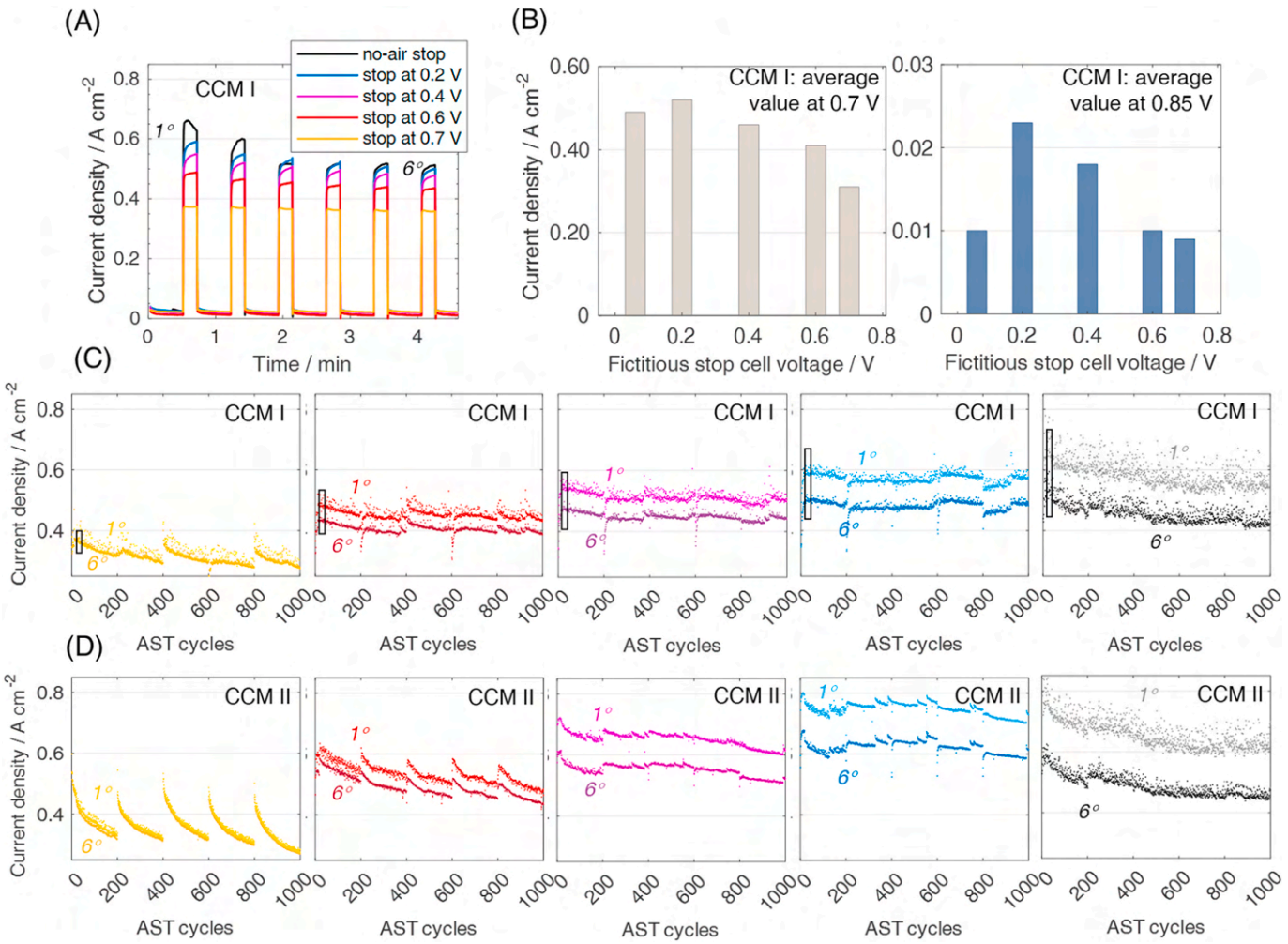

Fig. 4. (A) CCM I current density profile over 1 AST cycle at BoT (specifically, for the 20th cycle, evidenced by a black box in figure C, for different stop voltages. The six cycles between 0.85 V and 0.70 V are here shown; (B) Average value of the current density over the whole AST protocol for different stop potentials. Results are for the voltage level 0.70 V (left) and 0.85 V (right); (C-D) Current density profile over 1000 AST cycles at different stop voltages, for the first and the sixth setpoint at 0.7 V, as indicated in Fig. 3A. Every 200th cycles a long stop and the MEA characterization are performed. Results are referred to CCM I in figure C and to CCM II in figure D. Different colours correspond to different stop voltage cases, as in the legend of figure A.

that the estimated cathode potential E in Table 2 takes into account the only correction due to the HFR, while the contribution of ohmic losses in the catalyst layers is not included. The real cathode potentials are thus expected even higher than what estimated, in particular at the very low fictitious short-stop voltages of these tests. It is relevant that when the no-air stop was performed (black case), the performance of Fig. 4C and Fig. 4D continuously decreased over the time and no recovery was shown every 200th AST cycles, when the long stop and the cell state-of-health characterization were carried out. This is an indication that reversible effects are continuously cleaned under this protocol contrary to the other tests. When the stop is performed at 0.6 V or 0.7 V, a reversible degradation effect appeared and the current density undergoes a substantial improvement every 200th AST cycles. This trend is mainly ascribed to some Pt oxides that kept growing during the operation, temporarily decreasing the activity of the catalyst. Data interpretation for stops at 0.4 V and 0.2 V is complicated by more unstable profiles, probably consequence of water and thermal management, more critical at the combined high current densities and low cell voltages reached under these protocols. It is however important to emphasize that the relative difference between the 1st and 6th measured current is greater as the stop voltage is decreased in the range 0.4-0 V. It is suspected a more complete oxides removal in such a range, advantageous for the performance; on the other hand, Pt also appeared more destabilized consistently with the promoted rate of ECSA loss already presented in Fig. 3.

3.2.1. *Supplementary investigation on low voltage transitions*

The following experiments examine the influence of more frequent cycling conditions in comparison to the steady-state operation, both through the variation of the upper potential limit and of the lower potential limit. Indeed, the role of the minimum potential reached, revealed as critical in the previously reported fictitious stop transients, required to be further explored. The protocols were executed under hydrogen/diluted air ($x_{O2,dry} = 6.5\%$). Values were selected to span in a range relevant for both automotive and heavy-duty application: the reference potential window of this work, consisting in 0.85-0.70 V cycling, was modified by introducing variations that can be of hint in the design of the system operational constraints. First of all, we evaluated the range between 0.90 V and 0.70 V, as illustrated in Fig. 5A. Note that the stop was not included. An estimation of the electrode potential in each protocol, in dependence of the average drawn current (Figure SI5A), is in Table 3. The selection of the diluted conditions maintained the current densities sufficiently low such that the deviation between E and E_c is almost negligible.

As expected, the higher UPL is more detrimental in Fig. 5B. In a second comparison (Fig. 5C), the upper potential limit was kept at 0.85

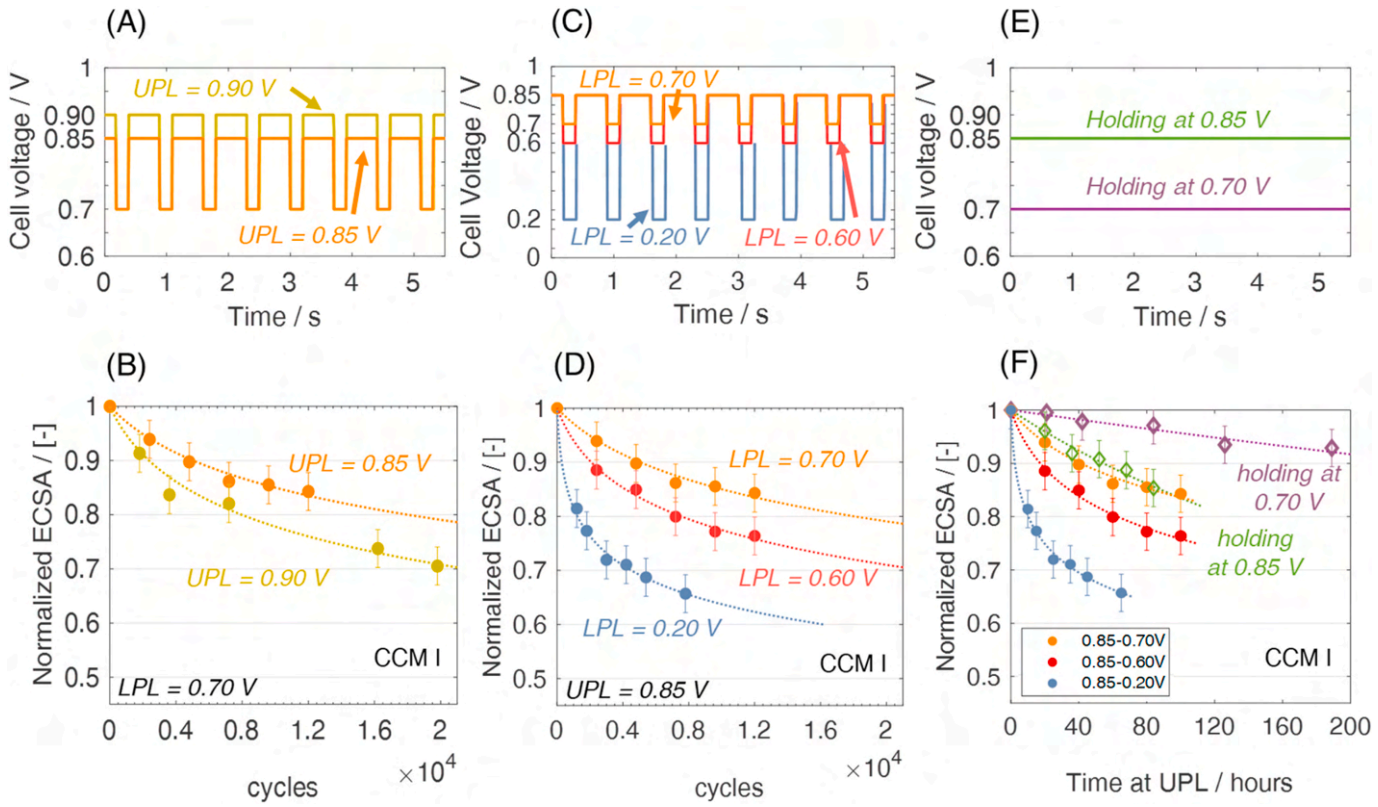

Fig. 5. (A) Applied square wave voltage profile for the accelerated protocol at different UPL; (B) Normalized ECSA decay with respect to the protocol cycles. Cycles between 0.70 V - 0.85 V and 0.70 V – 0.90 V are included, according to what reported in Fig. 5A; (C) Applied square wave voltage profile for the accelerated protocol at different LPL; (D) Normalized ECSA decay with respect to the protocol cycles. Cycling between 0.70 V and 0.85 V, 0.60 – 0.85 V and 0.20 V – 0.85 V are included, according to what reported in Fig. 5C; (E) Applied voltage holding profile at different voltages; (F) Normalized ECSA decay with respect to the time spent at the upper potential limit. Steady-state protocols at 0.70 V (purple) and at 0.85 V (green), as well as cycling between 0.70 V and 0.85 V (orange), 0.60 V – 0.85 V (red) and 0.20 V – 0.85 V (grey) are included.

Table 3
Table that summarizes the average current density over the whole AST protocol for different UPL and LPL values (carried out at 6.5% x_{O2} and at the controlled values of cell voltage E_c) and the cathode potential E estimated by correcting for the HFR.

E_c/V	Average current density/A cm^{-2}	Estimated E/V
Steady state at 0.70 V	0.33	0.71
Steady state at 0.85 V	0.004	0.85
Cycling 0.70 V–0.85 V	0.31–0.009	0.71–0.85
Cycling 0.70 V–0.90 V	0.31–0.001	0.71–0.90
Cycling 0.60 V–0.85 V	0.82–0.018	0.62–0.85
Cycling 0.20 V–0.85 V	1.36–0.041	0.23–0.85

V, while the lower potential was changed. The decrease of the LPL from 0.7 to 0.6 V was found deleterious too. After 12k cycles, the normalized ECSA is 84% and 76%, at LPL equal to 0.7 V and 0.6 V respectively (Fig. 5D). Quantitatively, the loss of these tests reasonably agree with Zihrul et al. [44]. As a term of comparison, the authors performed hydrogen/air square wave cycles of 30 s-30 s dwell time in the ranges 0.60–0.80 V and 0.60–0.90 V, identifying a retained ECSA around 80% and 57% after 12k cycles.

It is worth noting that in our experiments the ECSA profile is analogous between the cycling 0.70–0.90 V (Fig. 5B) and 0.60–0.85 V (Fig. 5D). From the point of view of the application, an increase of the maximum potential can be explored, which boosts the system efficiency, while the catalyst aging can be limited by avoiding too low cell potentials at the power peak. Most of all, this testing campaign evidenced an unexpected largely promoted degradation when the LPL is further reduced to 0.2 V. A sharp drop of the catalyst surface area appeared in this case, that made the normalized ECSA be 66% at 7.8k cycles. Coherently to the idea of a progressively enhanced surface cleaning from oxides, the average current drawn at 0.85 V got higher as long as the minimum voltage was reduced (Table 3 and Figure SI5.B).

To evidence the role of potential cycling, two different steady-state potentials (0.70 V and 0.85 V, Fig. 5E) were tested and compared against the previous results. Again, the decay in the electrochemically active surface area increased with the potential level. Restricting the potential to 0.70 V dramatically slows down the rate of loss, leading to an ECSA reduction of only 3% after 84 h, while the holding at 0.85 V lowers the ECSA of 15% after the same time (Fig. 5F). The faster decay of catalyst at increasing UPL is physically consistent to the incentivized Pt nanoparticles dissolution [50]. It is particularly noteworthy that, comparing the degradation induced by the steady-state 0.85 V and the voltage cycling between 0.85 V and 0.70 V, the loss is comparable with respect to the time spent at UPL, meaning that the holding at the maximum potential, and not the cycling, is the main stressor for the catalyst degradation. On the other hand, once the LPL is decreased from 0.70 V to 0.60 V, and even more to 0.20 V, we observed an incentivized aging. This loss, connected to the widest span of potentials, is attributed to the change of the surface coverage of Pt [23]: we can conclude that probably the extent of degradation is proportional to the degree of catalyst oxides reduction within a cycle, greater at 0.60 V and, more surprisingly, at 0.20 V.

3.3. Short-stop regulation: the impact of the scan rate and of the time spent at low potential

Once established the short-stop role, the parameters correlated to its

regulation were changed to assess the effect on the ECSA decay. The scan rate is studied in this section; we exploited the AST profile with a fictitious short-stop at 0.2 V. The hydrogen/diluted air operation ($x_{O2,dry}$ = 6.5%) allowed to control the transitions: a voltage change comparable to 5 mV s^{-1} was reproduced by a stair-case profile, which consisted in requiring to the load steps of 5 mV every second. Both the anodic and the cathodic transitions of the short-stop were investigated, according to the design of Fig. 6A and Fig. 6C.

In Fig. 6B, the decrease of the anodic scan has no impact on the ECSA decay, here directly compared to the step profile (already shown in Fig. 3B), indicated as "fast anodic scan". The scan rate effect on Pt dissolution is controversial in the literature. More fundamental studies on dissolution of Pt(111) showed a very small effect of the anodic scan rate [51], while Pavlišič et al. [52] proved that on a Pt-3 nm electrocatalyst the dissolution rate increased with the scan, consistently with the idea that the direct dissolution of Pt is more promoted if the surface is less oxidized in a fast process. However, the lower time spent in the transition decreased the total amount of dissolved Pt. In ASTs, Kneer et al. [33] saw that the impact of both the anodic and cathodic scan was minor. What we can conclude from our observations is that mitigation strategies that actively control the switch-on after stop would not be beneficial and that this transient has no influence on the aging observed for the potential profile here tested. Fig. 6C and Fig. 6D highlight the impact of different cathodic scans alongside the short-stop. Proceeding with a slow cathodic scan rate over the range 0.70-0.20 V seems slightly beneficial (compared to the "fast cathodic scan", the profile of Fig. 3). The span was then separated into the component between 0.70 V and 0.50 V and between 0.50 V and 0.20 V. While the former minorly varied compared to the previous case, the latter appeared a bit more detrimental, resulting in an additional 5% of ECSA loss at 1600 AST cycles. As a result, the overall slow cathodic scan (green profile of Fig. 6D) is showing a beneficial effect compared to the fast change between 0.70 V and 0.50 V (yellow profile), suggesting that proceeding slowly, mostly at $E_c \geq 0.5$ V, can be an valuable mitigation strategy.

To understand if these resulting profiles are also affected by the time spent in the low voltage range, we carried on tests with different stop durations. The profiles under analysis are depicted in Fig. 6E: they consist in the "standard" voltage cycling followed by a fictitious short-stop at the potentials of 0.4 V and 0.2 V. The short-stop duration was increased from 110 s to 220 s. The outputs are collected in Fig. 6F. Even though the main effect is attributed to the stop potential value, this analysis shows that the stop lasting can have a role: at 0.4 V, the longer is the time spent at the lowest voltage, the more promoted is the ECSA decay. At 0.4 V, the discrepancy between the holding times is more evident rather than at 0.2 V. This suggests that the time spent at the lowest potential has a greater influence as the voltage level gets higher.

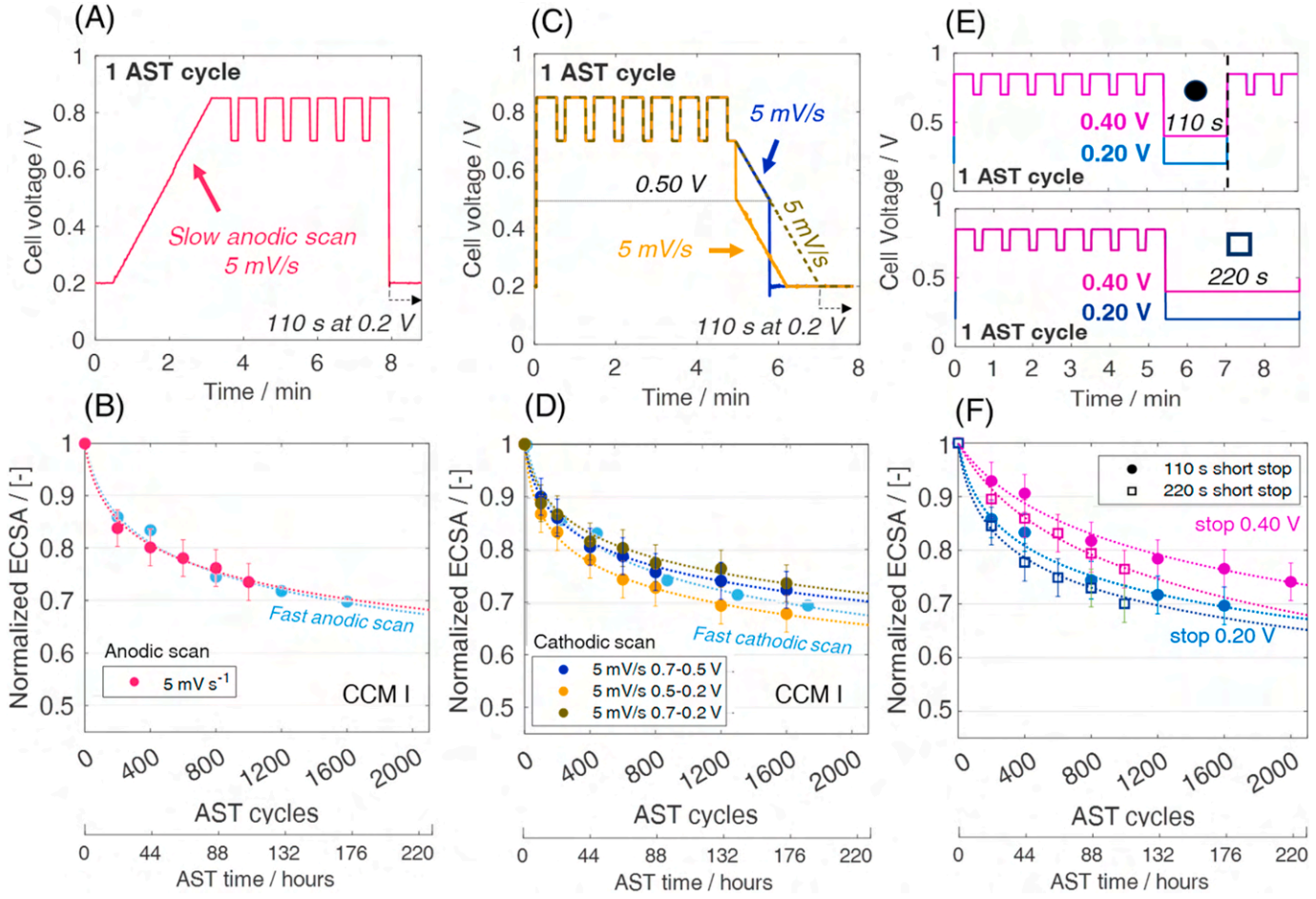

Fig. 6. (A) Voltage profile of the Accelerated Stress Test protocols at the slow anodic scan rate of 5 mV s^{-1} for the 0.2 V short-stop; (B) Normalized ECSA as a function of the protocol cycle for the voltage profile of figure A (slow anodic scan), with respect to the fast scan (square-wave, depicted in Fig. 3A); (C) Different voltage profiles of the Accelerated Stress Test protocols that exploit the slow cathodic scan rate of 5 mV s^{-1} for the short-stop; (D) Normalized ECSA as a function of the protocol cycle for the voltage profile of figure C (slow cathodic scans), with respect to the fast scan (square-wave, depicted in Fig. 3A); (E) Voltage profile of the Accelerated Stress Test protocols with different stop duration of 110 s and 220 s, at 0.4 V and at 0.2 V; (F) Normalized ECSA decay resulting from the voltage profiles of figure E with different stop durations.

3.4. Cathode gas humidification during stop

The effect of the humidification state of the short-stop transient is reported in Fig. 7. Nitrogen at 0% RH (not humidified, obtained by-passing the bubbler) was introduced at the beginning of the stop transient, while all the other AST parameters were kept unchanged. The objective was to test if a drying-out period during the stop was an advantage for mitigating catalyst aging, since the decrease of liquid water content can poor the Pt ions mobility. A resistive load was applied while a nitrogen flow rate equivalent to 0.6 NL min^{-1} was introduced at the end of the seventh period at 0.85 V of the cycle (Fig. 7A). As in the reference no-air stop profile (Fig. 2A), the potential is reduced with minor changes in dynamics. The short-stop duration was kept unchanged (110 s) but, at the half of this period, the nitrogen supply was interrupted to allow the cell potential reduction from ~0.15 V towards 0.06 V, as in the standard case. Following this procedure, possible differences in the results caused by unmatching minimum stop potentials were avoided.

Fig. 7B and Fig. 7C include the normalized ECSA for the dry stop protocol with respect to the standard case. The rate of decay of CCM I is almost unchanged, while for CCM II is reduced, leading to an improvement of 5% normalized ECSA at 1000 AST cycles.

3.5. Influence of the operational history: the upper potential limit

The following experiments examine the influence of the upper potential limit on the degradation of the catalyst layer in presence of no-air short-stops. Protocol voltage profiles are represented in Fig. 8A, 8C and 8E. They were performed in hydrogen/air and the results compared against the voltage cycling without short-stops, already presented in Section 3.2.1.

Starting from the reference AST, the Upper Potential Limit was changed in the range 0.70–0.90 V. For the case at 0.70 V, UPL and LPL coincided, implying a unique dwell time of 4.7 min at such a potential (additional information are in Table 4). The resulting ECSA decays are included in Fig. 8B, 8D and 8F as a function of the time spent at UPL. The normalized loss per cycle increased while increasing UPL both in presence and absence of short-stops. The decay was more rapid in the initial part of the protocol when the short-stop was frequently included; then, as a peculiar behaviour, the trend levelled off. The impact of low voltage transitions is clearly highlighted by this comparison. After 60 h at 0.85 V, the ECSA is lowered to 86% when stops are not introduced, while it drops to 65% in case they are inserted. After the same 60 h at 0.90 V, ECSA decreases to 82% in absence of stops, while to 56% if they are present. More surprisingly, the drop of ECSA significantly differs even at 0.70 V, being 98% and 79% without and with the short-stops respectively. Please, note that the decay in presence of stops (Fig. 8D) is even enhanced compared to all the outcomes of Fig. 5F, meaning that the no-air stops are responsible for an additional portion of aging.

Cross-sections of samples aged under UPL equal to 0.85 V and 0.90 V were also studied by SEM in comparison to the conditioned CCM I (Fig. 8G). Fig. 8H evidences that, once again, Pt band is not formed if the UPL is limited to 0.85 V. Here the protocol was carried out under hydrogen/air but the outcomes are consistent to Section 3.1, where the analogous voltage profile was performed under diluted air. Only when we increased the cell voltage towards 0.90 V, Pt precipitated in the membrane at a distance of approximately 1.2 mm from the cathode catalyst layer (Fig. 8I). In addition, it should be noted that even for this higher UPL no reduction of the electrode thickness was observed (Figure SI2C), suggesting that any possible carbon corrosion contribution is still minimal. Pt nanoparticles coarsening is therefore considered as the critical underlying process for the electrocatalyst degradation.

3.6. Influence of the operational history: the number of cycles

The voltage-controlled AST was modified in its high voltage cycling period to understand the specific role of the high voltage cycling with respect to the no-air short-stops. The profiles tested under hydrogen/air are illustrated in Fig. 9A. Specifically, the standard profile consisting in six cycles was varied to test one single transition while keeping unvaried the total time spent at 0.85 V. An additional test comprised only a fixed time at 0.85 V for 4.7 min, avoiding cycles in the operating window at all. Note that, in all these ASTs, the short-stops where equally "spaced" in time. The ECSA loss driven by these profiles (Fig. 9B) indicates that cycling at high potentials has a minor impact on catalyst surface aging as the no-air short-stop is recurring with the same time frequency. Only a minor dependence upon the cycles number can be observed (e.g. six cycles loss is minorly larger than one or zero cycles loss). This finding is consistent with Section 3.2.1, where we observed for this CCM that at $E_C \geq 0.70$ the catalyst loss is driven more by the UPL than by cycling. In brief, the graphic suggests that when the short-stop is frequently introduced, aging is controlled by this procedure rather than by the cycles of potential in the typical automotive operational range.

3.7. Influence of the operational history: the cathode gas feeding composition

The AST was tested under different cathode gas flow compositions: air, diluted air (6.5% O_2) and nitrogen. The profile consists in the voltage cycling between 0.7 and 0.85 V and the no-air short-stop (Fig. 10A). As clear, the dry oxygen mole fraction has a negligible impact since the decay trend in Fig. 10B is analogous between the pure and the diluted air case. Fig. 10C and Fig. 10D include the outcome of the profiles at 0.70 V, which confirm this observation. However, the electrode potential under hydrogen/air is larger than 0.70 V (see Table 5). Hence, to limit E to 0.70 V, E_c was controlled at 0.68 V while supplying diluted air. The resulting degradation is again relevant with respect to the 0.70 V holding, which confirms the importance of stopping. A case under inert environment is finally shown in Fig. 10E. When nitrogen is supplied, an Autolab® potentiostat is used to impose a ramp of 0.1 V s^{-1} in the cathodic transient to 0.06 V, while a ramp of 0.7 V s^{-1} for the faster

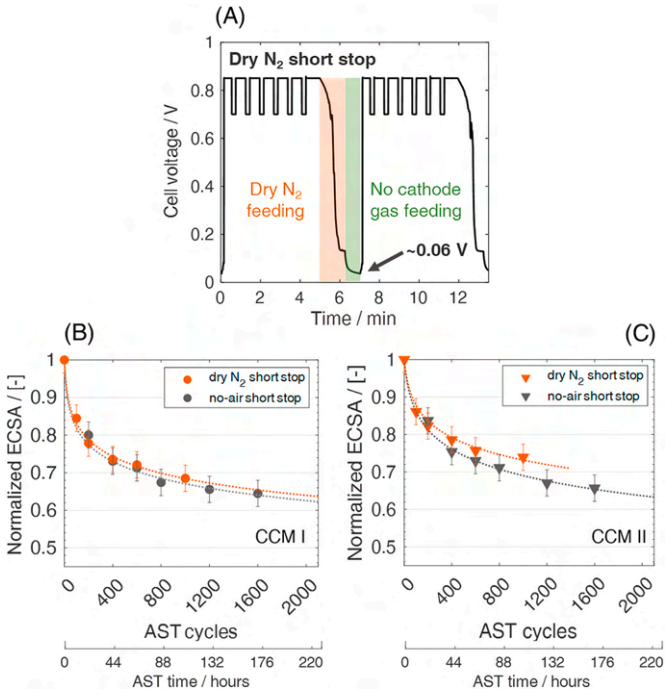

Fig. 7. (A) AST profile which includes the introduction of dry nitrogen for performing the short-stop; Normalized ECSA as a function of the AST cycles for the standard no-air short-stop protocol and for the dry nitrogen short-stop protocol: results are for (B) CCM I and (C) CCM II.

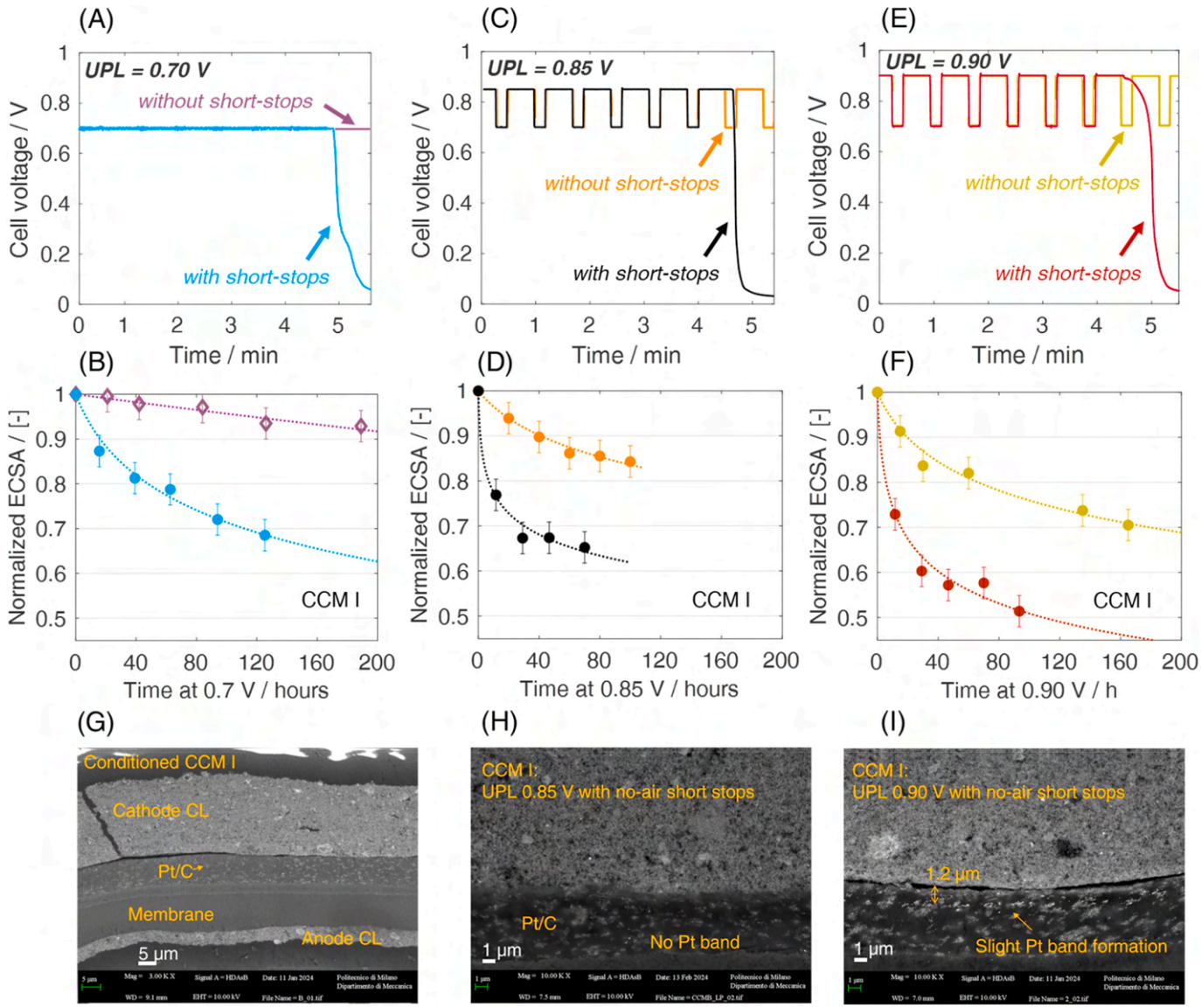

Fig. 8. Voltage profile and resulting normalized ECSA as a function of time spent at Upper Potential Limit for (A–B) Steady-state conditions at 0.70 V and case in which no-air short-stop is introduced every 4.7 min; (C–D) Square-wave cycling between 0.70 V and 0.85 V and case in which no-air short-stop is introduced every 6 cycles. (E–F) Square-wave cycling between 0.70 V and 0.90 V and case in which no-air short-stop is introduced every 6 cycles.
(G) SEM image of CCM I after the conditioning; (H) SEM image of CCM I aged under the accelerated protocol with no-air short stops, with an UPL of 0.85 V and (I) with an UPL of 0.90 V. Note that Pt/C is present in the pristine membrane. When the UPL is limited to 0.85 V, no clear Pt band is formed in the ionomer membrane. This is consistent to the findings of previous publications [26,27]. When the UPL is increased to 0.90 V, a slight Pt band is formed in the PEM close to the cathode catalyst layer: Pt precipitated at the distance of 1-1.5 µm from the interface with the cathode electrode.

Table 4
Table that summarizes the average current density over the whole AST protocol with different UPLs in presence of no-air short stops (carried out under hydrogen/air and at the controlled values of cell voltage E_c) and the cathode potential E, estimated by correcting for the HFR.

E_c /V	Average current density /A cm^{-2}	Estimated E /V
0.70–0.90	0.80–0.006	0.72–0.90
0.70	1.15	0.73

anodic transient between 0.06 V and 0.85 V, in order to be representative of the dynamics observed in the no-air procedure. The same value of 0.7 V s^{-1} is selected for performing the square wave profile in the high voltage region. The output of the H_2/N_2 protocol is included in Fig. 10F. It is relevant that the large ECSA loss due to the transients to the almost null cell voltage is present even under the inert atmosphere. A few discrepancies of the outputs between the nitrogen case and the O_2-rich cases could be attributed to the different cathode potential levels or to its uniformity across the electrode because of the drawn currents (e.g. the lower LPL seen by the catalyst layer under nitrogen could make the degradation over the voltage cycling between 0.85 V and 0.70 V slightly more impacting rather than under air, even though the aging experimental variation is extremely limited). These results suggest that (*i*) the high impact of short-stops subsists in tests carried out under an inert atmosphere, (*ii*) the degradation is reasonably consistent for different air dilutions.

3.8. Irreversible performance degradation analysis

Under ASTs, the cell performance is expected to deteriorate. The *operando* current density analysis presented in Section 3.2 is the

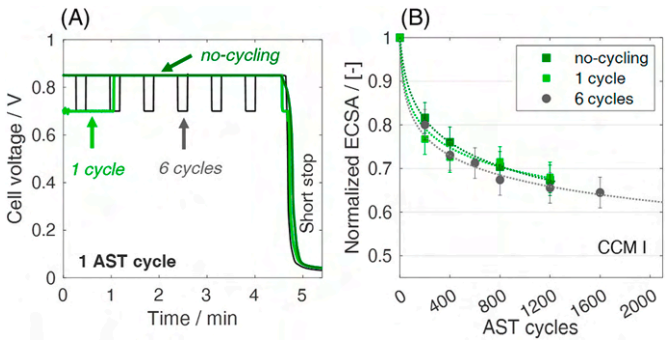

Fig. 9. (A) Voltage profile of the tested Accelerated Stress Test protocols with a different number of high voltage transitions (six, one or none) and in presence of no-air short-stops; (B) Normalized ECSA as a function of the protocol cycle and time under the ASTs depicted in figure A.

combination of two effects, namely the reversible and the irreversible loss. The first was mainly attributed to Pt oxides formation/reduction, since the protocols were specifically carried out at fully humidified or slightly oversaturated conditions for inhibiting ionomer degradation-related contributions (e.g. adsorption of sulfur or sulfonate groups on Pt [53] due to membrane chemical aging), which are enhanced at low relative humidity [54]. It should be however noted that the adsorption of the catalyst layer ionomer on the Pt surface can also have an impact on the *operando* ORR kinetics [55]. To focus on the irreversible loss only, polarization curves where periodically recorded. The voltage correspondent to some selected current densities was plotted *versus* the Pt roughness factor, which changes alongside aging because of the ECSA decay. The results of all the ASTs for CCM I are collected in Fig. 11A. At a given current density, the measured cell voltage well matches and follows the same path of variation, thus appearing as a prevalent function of catalyst r.f. It can be concluded that the Pt roughness factor, and hence the ECSA, is the critical responsible both for the kinetic loss, which dominates at low currents, and for the mass transport limitations [56], which rise up progressing towards high current densities. This analysis, as suggested by other authors [41], hints at the Pt dissolution/redeposition as the dominant underlying mechanism,

Table 5
Table that summarizes the average current density over the whole AST protocol for the controlled E_c values with different cathode gas feeding composition and in presence of no-air short-stops. Tests are under hydrogen/air, hydrogen/air diluted in nitrogen (6.5% $x_{O2,dry}$) and hydrogen/nitrogen. The estimated cathode potential E is also included.

E_c /V	Average current density /A cm^{-2}	Estimated E /V
0.68 V (diluted air)	0.61	0.70
0.70 V (air)	1.15	0.73
0.85–0.70 V (N_2)	0	0.85–0.70
0.85–0.70 (diluted air)	0.010–0.49	0.85–0.71
0.85–0.70 (air)	0.049–0.64	0.85–0.72

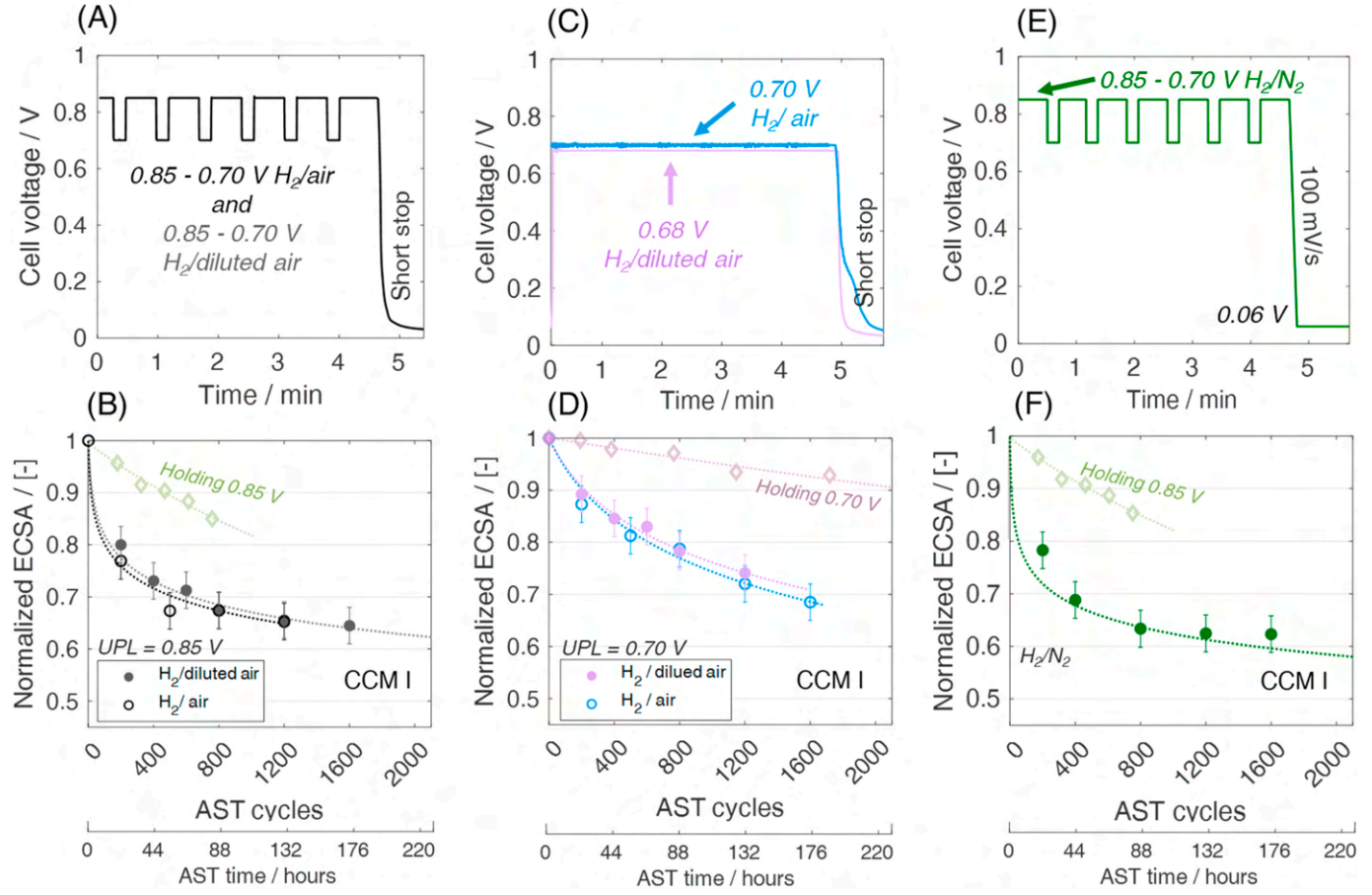

Fig. 10. Voltage profile of the Accelerated Stress Test protocols with a different cathode gas feeding composition (air, diluted air and nitrogen) in presence of short-stops. (A) Profile in case of maximum potential of 0.85 V; (B) Normalized ECSA as a function of the protocol AST in figure A and with different air dilutions; (C) Profile in case of maximum potential around 0.70 V; (D) Normalized ECSA as a function of the protocol AST in figure C and with different air dilutions; (E) AST profile under hydrogen/nitrogen; (F) Normalized ECSA as a function of the protocol under hydrogen/nitrogen of figure E. Constant voltage cases are included in the figures as a reference: they are compared on time basis.

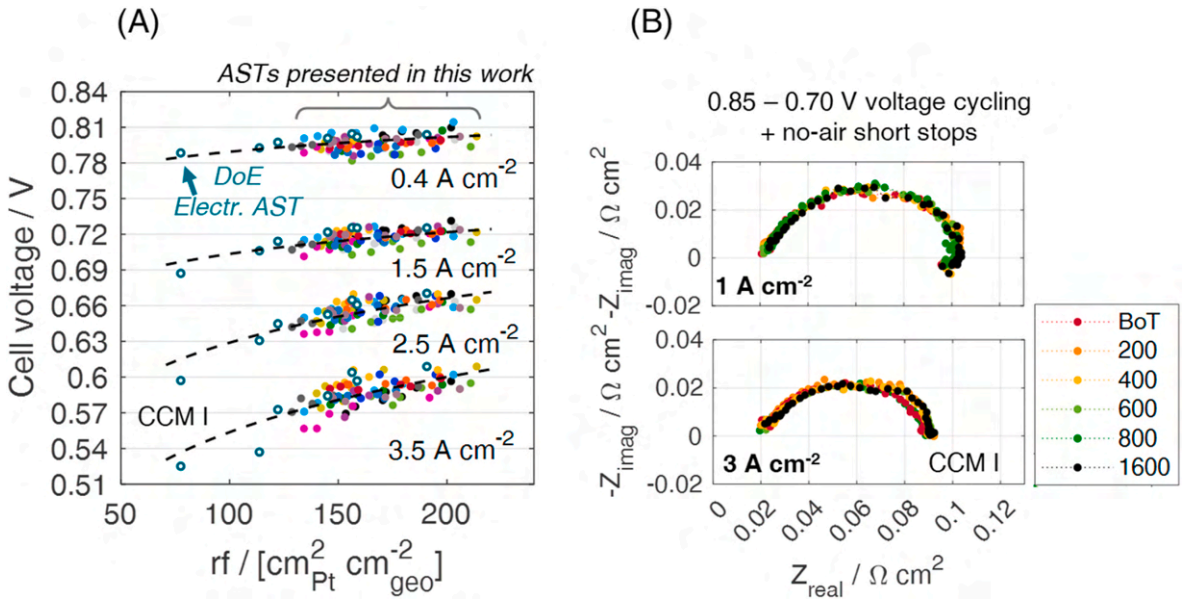

Fig. 11. (A) Cell voltage in H_2/air polarization curves for selected geometric current densities (0.4, 1.5, 2.5, 3.5 A cm^{-2}) as a function of the Pt catalyst roughness factor over aging under the various ASTs presented in this work. The measurements were performed under the operating conditions of the reference polarization curve. U.S. Department of Energy Electrocatalyst AST results are also included. The catalyst decay due to this protocol, consisting in 3s-3s cycles between 0.60-0.95 V, has been already presented in a previous publication [26]; (B) Nyquist plot recorded under at the current density of 1 A cm^{-2} (top) and 3 A cm^{-2} (bottom) under H_2/air reference polarization. Curves are for different cycles of the AST protocol with no-air short-stops, the outcomes of which were presented in *Section 3.1*.

consistently with the discussion of this work. In addition, Fig. 11B shows no relevant impact on the EIS Nyquist plots. Considering the constant HFR, membrane degradation was excluded. No significant deviations were recorded both in the high and in the low frequency range at the studied current densities (1 and 3 A cm^{-2}). Only a slight promotion of the low frequency resistance is observed. These results well agree with Pt nanoparticles coarsening as the critical degradation mechanism [57]. H_2/O_2 polarization curves are instead depicted in Figure SI6: in these conditions, the kinetic overpotentials are expected to dominate. The Tafel plot collects the HFR-corrected potential as a function of the specific current density of Pt surface. The current includes the contribution due to the hydrogen crossover and the short circuit, determined from the Linear Sweep Voltammetry [26]. In this measurement, the current density extrapolated at null voltage represents the contribution due to the hydrogen crossover, while the chart slope provides an estimation of the electric resistance, from which the shorting current is computed. Two independent CCM I samples were studied under the reference AST profile when no-air short-stops are included, both at BoT and after the application of 1600 cycles. At the Beginning, a Tafel slope of 74 ± 2 mV dec^{-1} was identified, which increased up to 84 ± 2 mV dec^{-1} at the end of the test. The observed Tafel slope at BoT exceeds the commonly assumed value of 70 mV dec^{-1}, which corresponds to a cathodic transfer coefficient of $\alpha_c = 1$ for the Oxygen Reduction Reaction, but it is still in agreement with literature findings [58]; after cycling it increased, as reported by other researchers in case of catalyst accelerated protocols [22]. In addition to the slope rotation, a shift towards higher specific current densities was observed. The result suggests that the specific Pt activity increases while decreasing the roughness factor. This output can be correlated to the growth of Pt NPs size and pairs to the slightly promoted Pt utilization factor (Section 3.1).

3.9. Discussion about the Pt degradation mechanism to explain the experimental results

The results of this study offer the chance to discuss the mechanism of catalyst degradation. Anyway, what included in this section has not to be considered exhaustive. Additional analyses are necessary, and some already planned, to elucidate the aging mechanism from a more fundamental point of view. The following considerations are based on the *in situ* and the *operando* electrochemical measurements of this work, combined with *post mortem* electron microscopy characterization. They are examined in relation to other recent literature findings: combined together, they can provide a broader picture of the electrocatalyst degradation issues.

This work established the impact of urban switch-offs in driving the irreversible Pt active surface area decay. In particular, we suspect a periodic reduction of platinum oxides in the low potential transients that enhances catalyst degradation, as exemplified in Fig. 12A. This is more stressed as the lower potential is progressively decreased from 0.7 V to 0 V: it can consistently explain the ECSA decay, signed by a larger rate of loss as the short-stop voltage gets lower (Fig. 3) and quantitatively indicated by the *k* parameter included in Fig. 12B (bottom). The removal of the oxidative layer in such a potential range agrees with the *operando* performance presented in Fig. 4. In more details, sufficiently long holding times at potentials ≥0.70 V can cause the formation of stable oxides, the removal of which could be responsible for the concomitant Pt dissolution in the cathodic scan. Note that an impact on the dissolution of the subsequent anodic transient may be present as well. The cathodic dissolution process can occur even at low potentials, which drive a fast Pt ions redeposition, at the basis of the relevant particle size increase shown by the TEM images (Fig. 2). Some literature works include findings that agree with this interpretation. Rice et al. [59] found different ECSA decays for the same AST protocol at a varying number of times the CV measurement was performed: larger particles were obtained as the frequency of the ECSA measurement increased. The authors suspected a promoted Pt dissolution/redeposition due to the reduction of stable place-exchanged oxides. Our outcomes interestingly suggest that stable oxides are formed even in the standard PEMFC operational range, when voltage clipping mitigation strategies are exploited, and that they require potentials lower than the most commonly accepted 0.6 V to be fully reduced. Such an outcome is in agreement with the recent works of Chattot et al. [60], who claimed that the place-exchange mechanism is initiated at potentials as low as 0.80 V_{RHE}, and of Ronovsky et al. [25], who showed that between 0.6 and 0.05 V a small number of catalytic sites, presumably highly oxophilic defects, are hardly reduced. Our suspect is that stable oxides might be

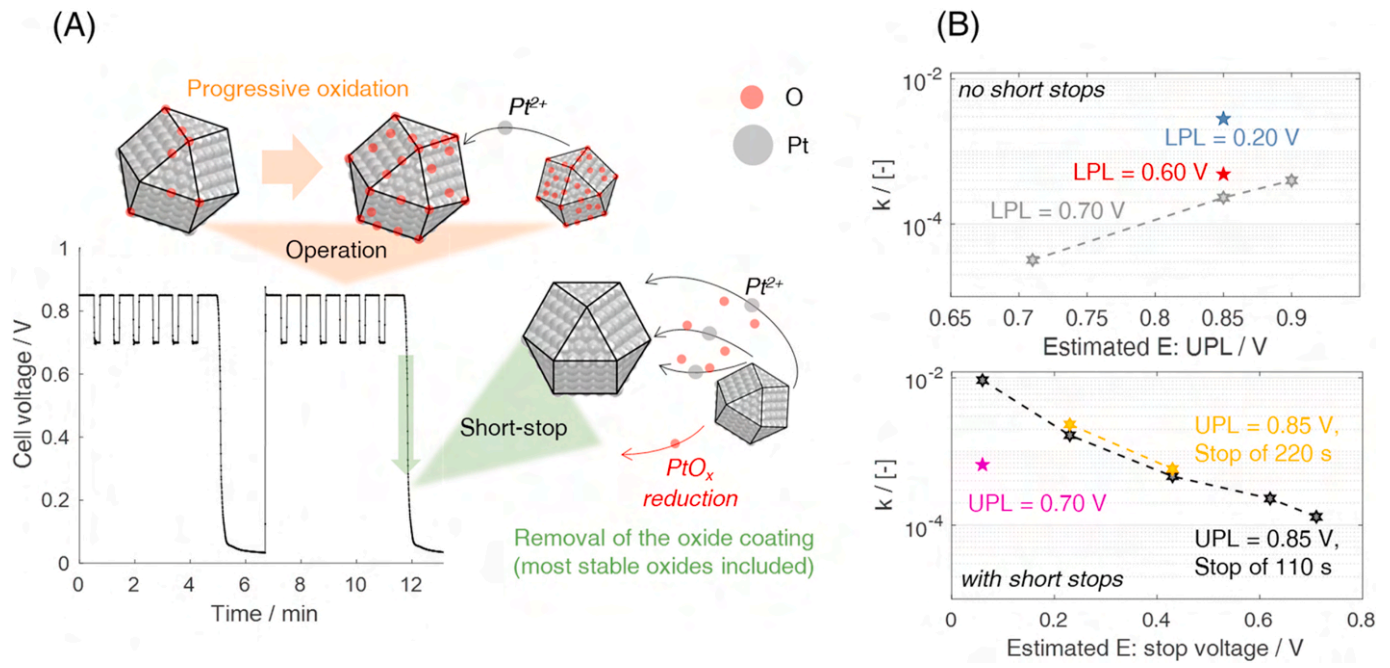

Fig. 12. (A) Schematic illustration of the proposed mechanism of degradation under the Accelerated Stress Tests studied in this work; (B) Top: trend of the k parameter with respect to the Upper Potential Limit in absence of short-stops, for three different LPL values. In order to obtain comparable parameters with respect to the bottom chart, which includes the outcomes of ASTs with short-stops, one cycle N in the fitting equation was selected equivalent to 6 cycles between UPL and LPL. This makes the cycling basis equivalent to 1 AST cycle in presence of short-stops. Bottom: trend of the k parameter with respect to the stop voltage, in presence of short-stops, and for different UPLs and stop durations. An uncertainty of ±10 mV on the x-axis must be considered.

even formed around 0.70 V, as Fig. 8 hints. In addition, a few recent literature works suggest the existence of a cathodic dissolution mechanism occurring during voltage transients at potentials lower than 0.6 V. Ahluwalia et al. [13] found a promoted Pt cathodic dissolution rate while reducing LPL from 0.4 V to 0.1 V, that may be attributed to a progressively oxide-free surface, even though the authors did not specifically comment the result. Sandbeck et al. [61,62] proved that, after having cycled the sample between 0.6 V and 1.5 V, the potential sweep towards 0.05 V caused an additional cathodic dissolution peak. They stated that the AST lower potential limit was too positive to remove all the oxides. Furthermore, they also evidenced the interesting size-dependence of the low voltage-cathodic dissolution, attributed to an increase of oxophilicity for the particles of small dimension [63], which can promote the formation of more stable oxides. Finally, Chattot et al. [64] synchronized the on-line Pt ions ICP-MS data with wide-angle X-ray scattering information, revealing a second cathodic dissolution peak (named C2) occurring just before and during the adsorption of hydrogen on Pt.

The effect of the UPL in absence of stops is summarized in Fig. 12B (top): the larger is the UPL, the more enhanced is the loss. When the LPL is reduced from 0.7 V to 0.6 V, and even more to 0.2 V, the rate of initial decay *k* jumps up. Similarly, the decrease of the short-stop potential to very low voltage values rises *k*. As explained, we suspect that the cathodic transients are the major contributors when the no-air stops are inserted. We expect the formation of stable oxides in the 4.7 min of the typical operational voltage window (0.70–0.85 V). Results of Fig. 9 indicate that minor difference subsists between 6 cycles, 1 cycle and no operational cycles, which suggest comparable stable oxide formation, hence cause of an analogous increase of Pt NP size. The outcomes are relevant for practical applications of the investigated CCM: less effort should be spent in terms of technological mitigation strategies on the frequency of the operational voltage transitions, while greater must be spent on the short-stop procedure. Consistently to our interpretation, the higher UPL in our protocols with short-stops (Fig. 8) is source for a higher oxidative layer formation and nanoparticles growth because of a possible cathodic dissolution. The interpretation agrees with the observed dominant Ostwald ripening mechanism rather than Pt ions precipitation into the membrane because of the gradient in the catalyst layer ionic potential due to hydrogen/air operation, which keeps the Pt ions on the cathode side [45]. Furthermore, in the cathodic ramp we expect an incentivized redeposition because of the very low voltage reached [65,66].

This work opens to the possibility of tuning the scan rate of cathodic transients for limiting aging (Fig. 6), mostly in the region between 0.5 V and 0.70 V. This may result from different combinations of oxides removal and/or Pt redeposition mechanisms. About the time spent at the minimum potential, catalyst surface degradation is more promoted as the time is higher since it can offer more room to the nanoparticles growth. About the role of an oxygen rich atmosphere, we concluded that dilution has no relevant impact on the mechanisms here studied (Fig. 10), but additional analyses will be carry out on this topic.

4. Conclusions

In this work, a wide dataset regarding hydrogen/air voltage cycling ASTs was presented. The degradation caused by voltage profiles in a range typical for the automotive PEM fuel cells (≤0.90 V) was studied, under operating conditions representative for the low power operation on two Pt/C CCM's. The effect of the voltage window and transients was assessed on the decay of the cathode catalyst active surface area. The ECSA loss during steady-state operation was significantly lower rather than under transient operation. As expected, the increase of the upper potential limit promoted the aging. However, when the maximum voltage was fixed at 0.85 V (a conventional voltage clipping in real systems), the lower potential limit was highlighted as critical.

When the voltage cycling was kept at potentials ≥0.7 V, the degradation was dominated by the time spent at the upper potential. The degradation was instead enhanced as the lower potential was reduced from 0.7 V to 0.6 V, consistently to literature interpretations about the progressive cleaning of a partially oxide-covered Pt surface.

Unexpectedly, transients to the cell voltage of 0–0.2 V caused a more promoted decay, which is the condition encountered during short-stops. The lower the short-stop potential, the larger the recovery of the reversible performance loss, but the larger the normalized ECSA drop. When the stop is introduced, the degradation is controlled by this transition rather than by cycling in the standard potential region (0.70–0.85 V). In addition, different short-stops parameters were tested. Mild effects of mitigation were identified working on the humidification state of the stop transients, using dry gas feeding, or on the cathodic potential sweep, by diminishing its value. The major attenuating effect was anyway obtained by increasing the minimum potential, even though at the expense of a higher reversible loss on the performance. Based on these results, the largest Pt nanoparticles coarsening likely happens during the cathodic sweeps of stops, even though alterations of the subsequent anodic transient cannot be excluded at all. The complete oxide removal seems to occur when the potential is reduced to very low values (<0.4 V), which could be attributed to the stripping of some stable oxides.

Declaration of competing interest

The authors declare that they have no known competing financial interests or personal relationships that could have appeared to influence the work reported in this paper.

Acknowledgments

The work was funded by Italian government (Ministero dell'Ambiente e della Sicurezza Energetica), in the frame of Progetto Permanent - Bando MITE PNRR Missione 2 Investimento 3.5 A - RSH2A_0O0012. The authors would like to thank Dr. Ludovica Rovatti (Mechanical Department, Politecnico di Milano) for her technical support with Scanning Electron Microscopy analysis. The authors thank also the students that contributed with some electrochemical investigation: Chiara Artini, Alessio Biffi and Alessandro Porta.

Appendix A. Supplementary data

Supplementary data to this article can be found online at https://doi.org/10.1016/j.ijhydene.2024.03.373.

References

[1] Pramuanjaroenkij A, Kakaç S. The fuel cell electric vehicles: the highlight review. Int J Hydrogen Energy 2023;48:9401–25. https://doi.org/10.1016/j.ijhydene.2022.11.103.
[2] Fan L, Tu Z, Chan SH. Recent development in design a state-of-art proton exchange membrane fuel cell from stack to system: Theory, integration and prospective. Int J Hydrogen Energy 2023;48:7828–65. https://doi.org/10.1016/j.ijhydene.2022.11.212.
[3] He W, Tang F, Li X, Zhang C, Ming P. Quantification and evolution on degradation mechanisms of proton exchange membrane fuel cell catalyst layer under dynamic testing conditions. Int J Hydrogen Energy 2023;48:18032–40. https://doi.org/10.1016/j.ijhydene.2023.01.109.
[4] Okonkwo PC, Ige OO, Barhoumi EM, Uzoma PC, Emori W, Benamor A, et al. Platinum degradation mechanisms in proton exchange membrane fuel cell (PEMFC) system: a review. Int J Hydrogen Energy 2021;46:15850–65. https://doi.org/10.1016/j.ijhydene.2021.02.078.
[5] Fan L, Zhao J, Luo X, Tu Z. Comparison of the performance and degradation mechanism of PEMFC with Pt/C and Pt black catalyst. Int J Hydrogen Energy 2022;47:5418–28. https://doi.org/10.1016/j.ijhydene.2021.11.135.
[6] Forouzandeh F, Li X, Banham DW, Feng F, Ye S, Birss V. Understanding the corrosion resistance of Meso- and micro-porous carbons for application in PEM fuel cells. J Electrochem Soc 2018;165:F3230–40. https://doi.org/10.1149/2.0261806jes.
[7] Shao-Horn Y, Sheng WC, Chen S, Ferreira PJ, Holby EF, Morgan D. Instability of supported platinum nanoparticles in low-temperature fuel cells. Top Catal 2007;46:285–305. https://doi.org/10.1007/s11244-007-9000-0.
[8] Plieth WJ. Electrochemical properties of small clusters of metal atoms and their role in surface enhanced Raman scattering. J Phys Chem 1982;86:3166–70. https://doi.org/10.1021/j100213a020.
[9] Tang Q, Li B, Yang D, Ming P, Zhang C, Wang Y. Review of hydrogen crossover through the polymer electrolyte membrane. Int J Hydrogen Energy 2021;46:22040–61. https://doi.org/10.1016/j.ijhydene.2021.04.050.
[10] Cherevko S, Kulyk N, Mayrhofer KJJ. Nano Energy Durability of platinum-based fuel cell electrocatalysts : dissolution of bulk and nanoscale platinum. Nano Energy 2016;29:275–98. https://doi.org/10.1016/j.nanoen.2016.03.005.
[11] Fuchs T, Drnec J, Calle-Vallejo F, Stubb N, Sandbeck DJS, Ruge M, et al. Structure dependency of the atomic-scale mechanisms of platinum electro-oxidation and dissolution. Nat Catal 2020;3:754–61. https://doi.org/10.1038/s41929-020-0497-y.
[12] Fuchs T, Briega-Martos V, Drnec J, Stubb N, Martens I, Calle-Vallejo F, et al. Anodic and cathodic platinum dissolution processes involve different oxide species. Angew Chemie - Int Ed 2023;62. https://doi.org/10.1002/anie.202304293.
[13] Ahluwalia RK, Papadias DD, Kariuki NN, Peng J-K, Wang X, Tsai Y, et al. Potential dependence of Pt and Co dissolution from platinum-cobalt alloy PEFC catalysts using time-resolved measurements. J Electrochem Soc 2018;165:F3024–35. https://doi.org/10.1149/2.0031806jes.
[14] Ehelebe K, Escalera-López D, Cherevko S. Limitations of aqueous model systems in the stability assessment of electrocatalysts for oxygen reactions in fuel cell and electrolyzers. Curr Opin Electrochem 2021;29:100832. https://doi.org/10.1016/j.coelec.2021.100832.
[15] O'Brien TE, Herrera S, Langlois DA, Kariuki NN, Yu H, Zachman MJ, et al. Impact of carbon support structure on the durability of PtCo electrocatalysts. J Electrochem Soc 2021;168:054517. https://doi.org/10.1149/1945-7111/abfe46.
[16] Yu K, Groom DJ, Wang X, Yang Z, Gummalla M, Ball SC, et al. Degradation mechanisms of platinum nanoparticle catalysts in proton exchange membrane fuel cells: the role of particle size. Microsc Microanal 2014;20:482–3. https://doi.org/10.1017/S1431927614004139.
[17] Karpenko-Jereb LV, Kovtunenko VA. Modeling of the impact of cycling operating conditions on durability of polymer electrolyte fuel cells and its sensitivity analysis. Int J Hydrogen Energy 2023;48:15646–56. https://doi.org/10.1016/j.ijhydene.2023.01.029.
[18] Seo D, Lee J, Park S, Rhee J, Choi SW, Shul YG. Investigation of MEA degradation in PEM fuel cell by on/off cyclic operation under different humid conditions. Int J Hydrogen Energy 2011;36:1828–36. https://doi.org/10.1016/j.ijhydene.2010.02.053.
[19] Rohendi D, Majlan EH, Mohamad AB, Daud WRW, Kadhum AAH, Shyuan LK. Effects of temperature and backpressure on the performance degradation of MEA in PEMFC. Int J Hydrogen Energy 2015;40:10960–8. https://doi.org/10.1016/j.ijhydene.2015.06.161.
[20] Đukić T, Moriau LJ, Pavko L, Kostelec M, Prokop M, Ruiz-Zepeda F, et al. Understanding the crucial significance of the temperature and potential window on the stability of carbon supported Pt-alloy nanoparticles as oxygen reduction reaction electrocatalysts. ACS Catal 2022;12:101–15. https://doi.org/10.1021/acscatal.1c04205.
[21] Yang Seungki, et al. Improvement of fuel cell durability performance by avoiding high voltage. Int J Automot Technol 2019;20:1113–21. https://doi.org/10.1007/s12239.
[22] Harzer GS, Schwämmlein JN, Damjanović AM, Ghosh S, Gasteiger HA. Cathode loading impact on voltage cycling induced PEMFC degradation: a voltage loss analysis. J Electrochem Soc 2018;165:F3118–31. https://doi.org/10.1149/2.0161806jes.
[23] Uchimura Masanobu, Sugawara Seiho, Suzuki Yosuke, Zhang Jianbo, Shyam S Kocha. Electrocatalyst durability under simulated automotive drive cycles. ECS Trans 2008;16:225–34. https://doi.org/10.1149/1.2981858.
[24] Zhang H, Haas H, Hu J, Kundu S, Davis M, Chuy C. The impact of potential cycling on PEMFC durability. J Electrochem Soc 2013;160:F840–7. https://doi.org/10.1149/2.083308jes.
[25] Ronovsky M, Pan L, Klingenhof M, Martens I, Chattot R, Fusek L, et al. Assessing utilization boundaries for Pt-based catalysts in an operating PEMFC. ACS Appl Energy Mater 2023;6(17):8660–5. https://doi.org/10.1021/acsaem.3c01243.
[26] Colombo E, Baricci A, Mora D, Guetaz L, Casalegno A. An innovative accelerated stress test representative of automotive PEMFC degradation mechanisms validated on 1000 hours real-world operation. J Power Sources 2023;580:233376. https://doi.org/10.1016/j.jpowsour.2023.233376.
[27] Colombo E, Baricci A, Bisello A, Guetaz L, Casalegno A. PEMFC performance decay during real-world automotive operation: evincing degradation mechanisms and heterogeneity of ageing. J Power Sources 2023;553:232246. https://doi.org/10.1016/j.jpowsour.2022.232246.
[28] Müller Bernd, et al. A new load cycle and durability test procedure based on vehicle fleet data. https://www.id-fast.eu/uploads/media/ID-FAST_Final_Workshop_2021-12-16_03_Drive_Cycle_public.pdf; 2021.
[29] Wilhelm F, et al. ID-FAST - analysis of coupling between mechanisms and definition of combined ASTs. https://www.id-fast.eu/uploads/media/ID-FAST_D4-3_Analysis_of_coupling_between_mechanisms_and_definition_of_combined_ASTs_OK.pdf; 2021.
[30] Hashimasa Y, Numata T. Comparison of test results on load cycle durability of polymer electrolyte fuel cell cathode catalysts. Int J Hydrogen Energy 2015;40:11543–9. https://doi.org/10.1016/j.ijhydene.2015.04.031.
[31] Ahluwalia RK, Wang X, Peng J-K, Konduru V, Arisetty S, Ramaswamy N, et al. Achieving 5,000-h and 8,000-h low-PGM electrode durability on automotive drive cycles. J Electrochem Soc 2021;168:044518. https://doi.org/10.1149/1945-7111/abf507.
[32] Borup R, Weber A, Ahluwalia RK, Mukundan R, Myers D, Neyerlin KC. M2FCT: million mile fuel cell truck consortium. DOE Hydrogen Fuel Cell Technologies Office 2023 Annual Merit Review and Peer Evaluation Meeting. 2023. http

s://www.hydrogen.energy.gov/docs/hydrogenprogramlibraries/pdfs/review23/fc339_weber_2023_o-pdf.pdf.
[33] Kneer A, Wagner N, Sadeler C, Scherzer A, Gerteisen D. Effect of dwell time and scan rate during voltage cycling on catalyst degradation in PEM. Fuel Cell 2018; 165:805–12. https://doi.org/10.1149/2.0651810jes.
[34] Kneer A. A semi-empirical catalyst degradation model based on voltage cycling under automotive operating conditions in PEM. Fuel Cell 2019;166:120–7. https://doi.org/10.1149/2.0641902jes.
[35] Astudillo L, Gasteiger H. Degradation of Pt-based cathode catalysts upon voltage cycling in single-cell PEM fuel cells under air or N2 at different relative humidities. J Electrochem Soc 2023;170:124512. https://doi.org/10.1149/1945-7111/ad10e9Manuscript.
[36] Colombo E, Bisello A, Casalegno A, Baricci A. Mitigating PEMFC Degradation During Start-Up: Locally Resolved Experimental Analysis and Transient Physical Modelling. J Electrochem Soc 2021;168:054508. https://doi.org/10.1149/1945-7111/abf4eb.
[37] Colombo E, Casadei D, Baricci A, Casalegno A. An open-source zero-gradient cell hardware to improve and accelerate durability testing of PEM Fuel Cell, under review. HardwareX 2023;16:e00495. https://doi.org/10.1016/j.ohx.2023.e00495.
[38] Tsotridis G, Pilenga A, Marco G De, Malkow T. EU harmonised test protocols for PEMFC MEA testing in single cell configuration for automotive applications. 2015. https://doi.org/10.2790/54653.
[39] Grimaldi A. Innovative design, modelling and control of a flexible fuel cell system for transport sector. PhD Dissertation Thesis. Politecnico di Milano; 2023. https://hdl.handle.net/10589/206693.
[40] Zhang X, Pisu P. Prognostic-oriented fuel cell catalyst aging modeling and its application to health-monitoring and prognostics of a PEM fuel cell. Int J Progn Heal Manag 2014;5:1–16. https://doi.org/10.36001/ijphm.2014.v5i1.2203.
[41] Della Bella RKF, Stühmeier BM, Gasteiger H. Universal correlation between cathode roughness factor and H 2/air performance losses in voltage cycling-based accelerated stress tests. J Electrochem Soc 2022;169:044528. https://doi.org/10.1149/1945-7111/ac67b8.
[42] Ferreira PJ, la O'GJ, Shao-Horn Y, Morgan D, Makharia R, Kocha S, et al. Instability of Pt/C electrocatalysts in proton exchange membrane fuel cells. J Electrochem Soc 2005;152:A2256. https://doi.org/10.1149/1.2050347.
[43] Takahashi T, Ikeda T, Murata K, Hotaka O, Hasegawa Shigeki, Tachikawa Y, et al. Accelerated durability testing of fuel cell stacks for commercial automotive applications: a case study. J Electrochem Soc 2022;169:044523. https://doi.org/10.1149/1945-7111/ac662d.
[44] Zihrul P, Hartung I, Kirsch S, Huebner G, Gasteiger HA. Voltage cycling induced losses in electrochemically active surface area and in H 2/air-performance of PEM. Fuel Cell 2016;163:492–8. https://doi.org/10.1149/2.0561606jes.
[45] Jahnke T, Baricci A, Rabissi C, Casalegno A. Physical modeling of catalyst degradation in low temperature fuel cells: platinum oxidation, dissolution, particle growth and platinum band formation. J Electrochem Soc 2020;167:149001. https://doi.org/10.1149/1945-7111/abbfda [J. Electrochem. Soc. , 167 , 013523 (2020)].
[46] Bisello A, Colombo E, Baricci A, Rabissi C, Guetaz L, Gazdzicki P, et al. Mitigated Start-Up of PEMFC in Real Automotive Conditions: Local Experimental Investigation and Development of a New Accelerated Stress Test Protocol. J Electrochem Soc 2021;168:054501. https://doi.org/10.1149/1945-7111/abf77b.
[47] Yu H, Baricci A, Bisello A, Casalegno A, Guetaz L, Bonville L, et al. Strategies to mitigate Pt dissolution in low Pt loading proton exchange membrane fuel cell: I. A gradient Pt particle size design. Electrochim Acta 2017;247:1155–68. https://doi.org/10.1016/j.electacta.2017.07.093.
[48] Ahluwalia RK, Arisetty S, Peng J, Subbaraman R, Wang X, Kariuki N, et al. Dynamics of particle growth and electrochemical surface area loss due to platinum dissolution, vol. 161; 2014. p. F291–304. https://doi.org/10.1149/2.051403jes. 3.
[49] Zago M, Baricci A, Bisello A, Jahnke T, Yu H, Maric R, et al. Experimental analysis of recoverable performance loss induced by platinum oxide formation at the polymer electrolyte membrane fuel cell cathode. J Power Sources 2020;455: 227990. https://doi.org/10.1016/j.jpowsour.2020.228316.
[50] Wang X, Kumar R, Myers DJ. Effect of voltage on platinum dissolution relevance to polymer electrolyte fuel cells. Electrochem Solid State Lett 2006;9:225–8. https://doi.org/10.1149/1.2180536.
[51] Topalov AA, Cherevko S, Zeradjanin AR, Meier JC, Katsounaros I, Mayrhofer KJJ. Chemical Science towards a comprehensive understanding of platinum dissolution in acidic media. 631–638. 2014. https://doi.org/10.1039/c3sc52411f.
[52] Pavliši A, Soc JE, Selih VS, Hodnik N, Gaberˇ M, Sala M. Platinum dissolution and redeposition from Pt/C fuel cell electrocatalyst at potential cycling. J Electrochem Soc 2018;165:F3161. https://doi.org/10.1149/2.0191806jes.
[53] Shinozaki K, Morimoto Y, Pivovar BS, Kocha SS. Suppression of oxygen reduction reaction activity on Pt-based electrocatalysts from ionomer incorporation. J Power Sources 2016;325:745–51. https://doi.org/10.1016/j.jpowsour.2016.06.062.
[54] Mitzel J, Zhang Q, Gazdzicki P, Friedrich KA. Review on mechanisms and recovery procedures for reversible performance losses in polymer electrolyte membrane fuel cells. J Power Sources 2021;488:229375. https://doi.org/10.1016/j.jpowsour.2020.229375.
[55] Kongkanand A. et al. Platinum surface oxide and oxygen reduction reaction kinetics during transient fuel cell operation platinum surface oxide and oxygen reduction reaction kinetics during transient fuel cell operation, J Electrochem Soc vol. 170; 2023. 094506. doi:10.1149/1945-7111/acfbbb.
[56] Liu S, Yuan S, Liang Y, Li H, Xu Z, Xu Q, et al. Engineering the catalyst layers towards enhanced local oxygen transport of Low-Pt proton exchange membrane fuel cells: materials, designs, and methods. Int J Hydrogen Energy 2023;48: 4389–417. https://doi.org/10.1016/j.ijhydene.2022.10.249.
[57] Baricci A, Zago M, Casalegno A. Modelling analysis of heterogeneity of ageing in high temperature polymer electrolyte fuel cells: insight into the evolution of electrochemical impedance spectra. Electrochim Acta 2016;222:596–607. https://doi.org/10.1016/j.electacta.2016.11.014.
[58] Lazaridis T, Gasteiger HA. Pt-catalyzed oxidation of PEMFC carbon supports: a path to highly accessible carbon morphologies and implications for start-up/shut-down degradation. J Electrochem Soc 2021;168:114517. https://doi.org/10.1149/1945-7111/ac35ff.
[59] Rice CA, Urchaga P, Pistono AO, McFerrin BW, McComb BT, Hu J. Platinum dissolution in fuel cell electrodes: enhanced degradation from surface area assessment in automotive accelerated stress tests. J Electrochem Soc 2015;162: F1175–80. https://doi.org/10.1149/2.0371510jes.
[60] Chattot R, Campos-roldàn C, Gasmi A, Stodel M, Martens I, Filhol J-S, et al. Paradigm shift of platinum oxidation below fuel cell open-circuit voltage. https://doi.org/10.21203/rs.3.rs-3366519/v1; 2023.
[61] Sandbeck DJS, Secher NM, Speck FD, Sørensen JE, Kibsgaard J, Chorkendorff I, et al. Particle size effect on platinum dissolution: considerations for accelerated stability testing of fuel cell catalysts. ACS Catal 2020;10:6281–90. https://doi.org/10.1021/acscatal.0c00779.
[62] Sandbeck DJS, Secher NM, Inaba M, Quinson J, Sørensen JE, Kibsgaard J, et al. The dissolution dilemma for low Pt loading polymer electrolyte membrane fuel cell catalysts. J Electrochem Soc 2020;167:164501. https://doi.org/10.1149/1945-7111/abc767.
[63] Mayrhofer KJJ, Blizanac BB, Arenz M, Stamenkovic VR, Ross PN, Markovic NM. The impact of geometric and surface electronic properties of Pt-catalysts on the particle size effect in electrocatalysis. J Phys Chem B 2005;109:14433–40. https://doi.org/10.1021/jp051735z.
[64] Chattot R, Mirolo M, Martens I, Kumar K, Martin V, Gasmi A, et al. Beware of cyclic voltammetry! Measurement artefact in accelerated stress test of fuel cell cathode revealed by operando X-ray diffraction. J Power Sources 2023;555:232345. https://doi.org/10.1016/j.jpowsour.2022.232345.
[65] Lopes PP, Tripkovic D, Martins PFBD, Strmcnik D, Ticianelli EA, Stamenkovic VR, et al. Dynamics of electrochemical Pt dissolution at atomic and molecular levels. J Electroanal Chem 2018;819:123–9. https://doi.org/10.1016/j.jelechem.2017.09.047.
[66] Pizzutilo E, Geiger S, Grote J-P, Mingers A, Mayrhofer KJJ, Arenz M, et al. On the need of improved accelerated degradation protocols (ADPs): examination of platinum dissolution and carbon corrosion in half-cell tests. J Electrochem Soc 2016;163:F1510–4. https://doi.org/10.1149/2.0731614jes.